Daytime variation of aerosol indirect effect for warm marine boundary layer clouds in the eastern north Atlantic

Shaoyue Qiu[1], Xue Zheng[1], David Painemal[2,3], Christopher R. Terai[1], and Xiaoli Zhou[4,5]

[1]Atmospheric, Earth and Energy Division, Lawrence Livermore National Laboratory, Livermore, California, USA
[2] Science Directorate, NASA Langley Research Center, Hampton, VA, USA
[3] Analytical Mechanics Associates, Hampton, VA, USA
[4]Chemical Sciences Laboratory, NOAA, Boulder, CO, USA,
[5]Cooperative Institute for Research in Environmental Sciences (CIRES), University of Colorado, Boulder, CO, USA

Correspondence to: Shaoyue Qiu (qiu4@llnl.gov)

Abstract. Warm boundary layer clouds in the Eastern North Atlantic region exhibit significant diurnal variations in cloud properties. However, the diurnal cycle of the aerosol indirect effect (AIE) for these clouds remains poorly understood. This study takes advantage of recent advancements in the spatial resolution of geostationary satellites to explore the daytime variation of AIE by estimating the cloud susceptibilities to changes in cloud droplet number concentration (N_d). Cloud retrievals for four months of July (2018-2021) from SEVIRI on Meteosat-11 over this region are analyzed. Our results reveal a significant "U-shaped" daytime cycle in susceptibilities of cloud liquid water path (LWP), cloud albedo, and cloud fraction. Clouds are found to be more susceptible to N_d perturbations at noon and less susceptible in the morning and evening. The magnitude and sign of cloud susceptibilities depend heavily on the cloud state defined by cloud LWP and precipitation conditions. Non-precipitating thin clouds account for 44% of all warm boundary layer clouds in July and they contribute the most to the observed daytime variation. Non-precipitating thick clouds are the least frequent cloud state (10%), they exhibit more negative LWP and albedo susceptibilities compared to thin clouds. Precipitating clouds are the dominant cloud state (46%), but their cloud susceptibilities show minimal variation throughout the day.

We find evidence that the daytime variation of LWP and albedo susceptibilities for non-precipitating clouds are influenced by a combination of the diurnal transition between non-precipitating thick and thin clouds and the "lagged" cloud responses to N_d perturbations. The daytime variation in cloud fraction susceptibility for non-precipitating thick clouds can be attributed to the daytime variation in cloud morphology (e.g., overcast or broken). The dissipation and development of clouds do not adequately explain the observed variation in cloud susceptibilities. Additionally, daytime variation of cloud susceptibility is primarily driven by variation in the intensity of cloud response rather than the frequency of occurrence of cloud states. Our results imply that polar-

38   orbiting satellites with overpass time at 13:30 local time underestimate daytime mean value of cloud susceptibility,

39   as they observe susceptibility daily minima in the study region.

40
41

1. Introduction

Warm boundary layer clouds, including stratus, stratocumulus, and cumulus clouds, are prevalent over the sub-tropical oceans, account for over 30% of the global annual mean cloud coverage (Warren et al., 1988; Wood, 2012). These clouds have a significant net negative radiative forcing on the surface radiation budget. However, our understanding of the aerosol indirect effect (AIE) on these clouds, particularly the impact of aerosols on cloud amount, brightness, and lifetime, remains a significant source of uncertainty in estimating the radiative forcing from human activities. The AIE plays a critical role in the Earth's radiation budget through its interactions with clouds. It consists of two effects: the Twomey effect, which involves the increase in cloud droplet number from increasing aerosols, and leads to an increase in cloud albedo (α_c) from smaller droplets when the cloud liquid water path (LWP) is held constant (Twomey, 1977), and the cloud adjustment effect, which encompasses the impact of aerosols on cloud amount, cloud water, and α_c through modulating cloud processes (e.g., Albrecht, 1989; Xue and Feingold, 2006; Chen et al., 2014; Gryspeerdt et al., 2019). The cloud adjustment effect is highly variable with large uncertainties in signs and magnitudes depending on cloud state, boundary layer, and meteorological conditions among other factors (e.g., Han et al., 2002; Wang et al., 2003; Small et al., 2009; Sato et al, 2018).

Previous studies have made significant progress in identifying different cloud processes and feedback mechanisms to explain the responses of CF, LWP, and α_c to aerosol perturbations (e.g., as summarized in Steven and Feingold, 2009; Fan et al., 2016; Gryspeerdt et al., 2019). The cloud adjustment effect is influenced by two key feedback mechanisms: precipitation suppression, and sedimentation-evaporation-entrainment.

Under clean conditions and for clouds predominantly precipitating, an increase in the cloud droplet number concentration (N_d) and associated decrease in droplet sizes, reduces precipitation efficiency, and decreases water loss from precipitation. Consequently, this promotes an increase in cloudiness and cloud LWP (Albrecht, 1989; Qian et al., 2009; Li et al., 2011; Terai et al., 2012, 2015). For non-precipitating clouds, decreased cloud drop size due to increases in N_d impacts CF and LWP through their impact on the entrainment rate. A decrease in cloud droplet size diminishes the sedimentation rate in clouds, causing an accumulation of cloud water near the cloud top. This increased cloud water in the entrainment zone enhances cloud-top radiative cooling, entrainment rate, and evaporation, resulting in a decrease in CF and cloud LWP (Bretherton et al., 2007; Chen et al., 2014; Toll et al., 2019; Gryspeerdt et al., 2019).

Additionally, the faster evaporation rates from smaller droplets enhance cloud-top cooling, downward motion in clouds, total kinetic energy, and horizontal buoyancy gradient. The processes listed above, in turn, increase evaporation and entrainment rate and, thus, forming a positive feedback loop (Wang et al., 2003; Xue and Feingold, 2006; Small et al., 2009; Toll et al., 2019). Furthermore, among non-precipitating clouds, thick clouds with larger LWP exhibit stronger cloud-top longwave radiative cooling rate and therefore stronger cloud-top entrainment rate (e.g., Sandu et al., 2008, Williams and Igel, 2021). Therefore, the classification of cloud states (e.g., precipitating conditions and thickness) is essential for accurately quantifying the AIE and discerning opposing cloud processes. In this study, we classify cloud states based on the LWP-N_d parameter space, as these variables provide the most informative metrics for cloud susceptibility (Zhang et al., 2022).

78   This study focuses on the Eastern North Atlantic (ENA) region, where the U.S. Department of Energy

79   (DOE) Atmospheric Radiation Measurement program (ARM) deployed the ground-based user facility at the Azores

80   archipelago (Mather and Voyles, 2013). During the summer over ENA region, warm boundary layer clouds exhibit

81   pronounced diurnal variations in their properties and cloud states. For example, based on ARM surface radar and

82   lidar observations, the frequency of stratocumulus clouds is highest at night, accompanied by an increase in the

83   fraction of precipitating clouds. Throughout the daytime, both cloud fraction and precipitation fraction experience a

84   slight decrease, followed by an increase after sunset (Remillard et al, 2012). The retrieved cloud microphysical

85   properties from ARM ground-based observations show similar "U-shaped" diurnal variations in cloud LWP, liquid

86   water content, and optical thickness (Dong et al., 2014). Additionally, numerical studies have revealed a distinct

87   diurnal cycle of AIE for marine stratocumulus clouds, attributed to changes in cloud properties and boundary layer

88   thermodynamic conditions (e.g., Sandu et al., 2008, 2009). However, observational analyses based on the ground-

89   based observations at the ENA site or in-situ measurements from field campaigns are often based on a few cases

90   with limited samples and insufficient spatial coverage (e.g., Liu et al., 2016; Wang et al., 2021; Zheng et al., 2022).

91   There have been few observational studies investigating the diurnal cycle of AIE in the ENA region. With recent

92   advancements in the spatial resolution of geostationary satellites, this study aims to investigate the diurnal variation

93   of the AIE in warm boundary layer clouds over the ENA region and gain a better understanding of the underlying

94   mechanisms.

95   Both cloud properties and meteorological conditions have substantial spatiotemporal variability and distinct

96   diurnal variations. Furthermore, changes in meteorological conditions can in turn influence cloud and aerosol

97   properties. One of the main challenges in understanding the AIE lies in isolating the impacts of the confounding

98   meteorological drivers on clouds and aerosols from AIE on clouds. To address this challenge, Gryspeerdt et al.

99   (2016) proposed the use of N_d as an intermediary variable for AIE, instead of using aerosol optical depth (AOD) or

100   aerosol index. The use of N_d circumvents the well-known dependency of AOD on CF and surface wind speed,

101   which does not necessarily reflect actual changes in aerosol loading. Moreover, the control of relative humidity and

102   aerosol type on AOD prevents to establish a direct link between AOD and aerosol concentration or cloud

103   condensation nuclei (CCN).

104   Another common method to disentangle meteorological impacts is to sort the controlling meteorological

105   factors of cloud state, such as relative humidity, lower tropospheric stability, vertical velocity, and examine the AIE

106   accordingly (e.g., Chen et al., 2014; Gryspeerdt et al., 2019). However, this approach overlooks important

107   information, including the frequency of occurrence of specific environmental conditions, the spatiotemporal co-

108   variation of meteorological factors, and the correlations among them. Zhou et al. (2021) and Zhang et al. (2022)

109   proposed a new method to estimate the cloud susceptibility within a confined space (e.g., a $1° \times 1°$ or $2° \times 2°$ grid

110   box) of each satellite snapshot by assuming consistent meteorological conditions within this spatial domain.

111   Additionally, it is important to note that meteorological conditions influence albedo susceptibility by altering the

112   frequency of occurrence of different cloud states (e.g., precipitating and non-precipitating). Specifically, within a

113   particular cloud state, meteorological conditions offer limited information regarding cloud susceptibility (Zhang et

114   al, 2022).

115   The second main source of uncertainty in observational AIE studies arise from inferring processes in a

116   temporally evolving system based on snapshots of observations (Mülmenstädt and Feingold, 2018). Due to the

117   limited temporal or spatial resolution of the observations, most studies assume a Markovian system, where clouds

118   and AIE are assumed to only relate to the current state of the system and have no memory of the past states.

119   However, this assumption contradicts the nature of the cloud system. Observational and modeling studies have

120   shown that aerosol-cloud interaction processes take hours to reach the equilibrium state and the sensitivity of AIE is

121   time dependent. For instance, Glassmeier et al. (2021) applied a Gaussian-process emulation and derived the

122   adjustment equilibration timescale for LWP to be ~20 hours. By tracking the ship tracks in satellite observations,

123   Gryspeerd et al. (2021) found a similar AIE timescale of ~20 hours or longer and the magnitude of LWP

124   susceptibility increases with time. In addition, Christensen et al. (2020) discovered that influence of aerosols on

125   cloud LWP, CF, and cloud top height persists two to three days by tracking cloud systems in satellite observations.

126   In summary, the sensitivity of cloud responses to N_d perturbations changes with time and, thus, the assumption that

127   AIE has no memory of its past state is inadequate. Nonetheless, the direct evaluation of the impact of cloud memory

128   on the quantified cloud susceptibility remains unexplored, to the best of our knowledge.

129   To facilitate a process-level understanding of the drivers behind the diurnal variation of AIE for warm

130   boundary layer clouds, we will classify these clouds into three states: precipitating clouds, non-precipitating thick

131   clouds, and non-precipitating thin clouds. We investigate the changes in both the frequency of occurrence of cloud

132   states and the magnitude of AIE for different cloud states throughout the day. Additionally, we document the

133   temporal changes in cloud state within each fixed $1° \times 1°$ grid box and quantify the influences of cloud memory and

134   state transition on AIE. Section 2 describes the datasets as well as the methodology employed to quantify cloud

135   susceptibilities, distinguish precipitating clouds from the satellite retrievals, and track cloud states. We present our

136   results in Section 3. Section 3.1 characterizes the general conditions of warm boundary clouds over the ENA region

137   during the summer. Section 3.2 introduces the LWP-N_d parameter space and illustrates the dependence of cloud

138   responses to N_d perturbations on cloud states. We then discuss the mean daytime variation of cloud susceptibilities

139   for all cloud states in Section 3.3, followed by an analysis of the AIE daytime variation for each cloud state and the

140   impact of the state transition on AIE in Section 3.4. In Section 3.5, we decompose the contributions to the daytime

141   variation of cloud susceptibility into two components, one is from changes in the frequency of occurrence of

142   different cloud states and the other is from changes in the intensity of AIE during the day. Section 4 includes

143   discussions on the similarities and differences in findings between this study and previous studies of AIE and

144   Section 5 is the summary and conclusions of this study.

145   **2. Dataset and Methodology**

146   We use cloud retrievals derived from the Spinning Enhanced Visible InfraRed Imager (SEVIRI) on

147   Meteosat-11, with a spatial resolution of 3 km at nadir and a half-hourly temporal resolution over the ENA region

148   (33-43°N, 23-33°W). SEVIRI cloud products are derived using the Satellite ClOud and Radiation Property retrieval

149   System (SatCORPS) algorithms (e.g., Painemal et al., 2021), based on the methods applied by the Clouds and the

150 Earth's Radiant Energy System (CERES) project, and specifically tailored to support the ARM program over the

151 ARM ground-based observation sites (Minnis et al. 2011, 2020). Given the purpose of this study on quantifying the

152 AIE on warm boundary layer clouds, we focus on four months of July (2018-2021), a period that coincides with the

153 highest frequency of occurrence of warm boundary layer clouds over the ARM ENA site (Rémillard et al. 2012;

154 Dong et al., 2014, 2023).

155 The cloud mask algorithm implemented in SatCORPS is described in Trepte et al. (2019). SatCORPS cloud

156 properties are based on the shortwave-infrared split-window technique during daytime (VISST, Minnis et al. 2011,

157 2020), with cloud optical depth (τ) and effective radius (r_e) being derived using an iterative process that combines

158 reflectance and brightness temperatures from the 0.64 μm and 3.9 μm channels. Cloud LWP is computed from τ and

159 r_e using the formula $LWP = \frac{4r_e\tau}{3Q_{ext}}$, where Q_{ext} represents the extinction efficiency and assumed constant of 2.0

160 (Minnis et al. 2011, 2020). The top-of- atmosphere (TOA) broadband shortwave α_c is derived from an empirical

161 radiance-to-broadband conversion using the satellite imager's visible channel and CERES Single Scanning Footprint

162 (SSF) shortwave fluxes, and dependent on solar zenith angle and surface type (Minnis et al. 2016). Cloud top height

163 computation follows the methodology in Sun-Mack et al. (2014).

164 To validate the Meteosat-11 retrieved cloud mask and the detection of boundary layer clouds, we compare

165 the boundary layer cloud fractions derived from Meteosat-11 with the ground-based observations at the ARM ENA

166 site. As seen in Fig.S1, both the diurnal variation and the mean CF of Meteosat-11 agree well with ARM

167 observations. More details on the methodology for the evaluation study are included in the supplementary material.

168 Our analysis focuses on warm boundary layer clouds with cloud tops below 3km and a liquid cloud phase.

169 To focus specifically on boundary layer cloud cases without including the edges of deep clouds, we apply a stricter

170 threshold than merely using the pixel-level cloud top height. We define boundary layer clouds as those with 90% of

171 their cloud tops below 3km, labeling all contiguous cloudy pixels as distinct cloud objects.

172 Cloud N_d is retrieved based on the adiabatic assumptions for warm boundary layer clouds, as in Grosvenor

173 et al. (2018) according to the following equation:

174 $$N_d = \frac{\sqrt{5}}{2\pi k}\left(\frac{f_{ad}c_w\tau}{Q_{ext}\rho_w r_e^5}\right)^{1/2} \tag{1}$$

175 In Equation (1), k represents the ratio between the volume mean radius and r_e, assumed to be constant of 0.8 for

176 stratocumulus; f_{ad} is the adiabatic fraction of the observed liquid water path and assumed to be 0.8 for

177 stratocumulus clouds (Brenguier et al., 2011; Zuidema et al., 2012); c_w is the condensation rate, which is a function

178 of temperature and pressure; Q_{ext} is the extinction coefficient, approximated as 2 in this study; and ρ_w is the density

179 of liquid water. While the different components of Eq. (1) could contribute to the uncertainties in N_d, errors in r_e are

180 the dominant drivers in Eq. (1) (Grosvenor et al., 2018).

181 To minimize uncertainties associated with bias in satellite cloud microphysical retrievals, we only select

182 pixels with a minimum r_e of $3\mu m$, a minimum τ of 3, and a solar zenith angle (SZA) of less than 65° (e.g., Painemal

183 et al., 2013; Painemal, 2018; Zhang et al., 2022). The SZA threshold of 65° was chosen to minimize biases observed

184 at high solar zenith angle in r_e and τ (e.g., Grosvenor & Wood, 2014; Grosvenor et al., 2018).

185   In addition, to reduce uncertainties associated with the adiabatic assumption in the N_d retrieval, we

186   implement a filtering process. For each cloud, we exclude cloudy pixels at the cloud edge, defined as those adjacent

187   to cloud-free pixels, following a similar sampling strategy suggested by Gryspeerdt et al. (2022). Therefore, all

188   cloud properties in this study refer to the properties of cloud body without cloud edge. It is worthy of note that

189   shallow cumulus clouds with diameters smaller than 9km are not included. The removal of cloud-edge pixels

190   accounts for ~14% of the cloudy pixels. Furthermore, we removed grid boxes containing islands due to the

191   uncertainties in Meteosat retrievals over contrasting underlying surface. Lastly, to avoid unrealistically large

192   retrievals, we eliminate pixels with the retrieved N_d values exceeding $1000\ cm^{-3}$, which constituted only 0.002% of

193   the data.

194   Cloud susceptibility is quantified as the slope between cloud properties and N_d using a least-square

195   regression. As found by Arola et al. (2022) and Zhou and Feingold (2023), the retrieved cloud susceptibilities are

196   sensitive to small-scale cloud heterogeneity, the co-variability between cloud properties and N_d, and the spatial scale

197   of cloud organization. To reduce biases resulting from heterogeneity and co-variability, we first average the 3-km

198   pixel-level cloud retrievals and N_d (Eq. 1) to a regular $0.25° \times 0.25°$ grid for each half-hourly time step.

199   To further mitigate the impact from co-variability between cloud properties and N_d at larger spatiotemporal

200   scales, cloud susceptibility is estimated within a $1° \times 1°$ grid box at each satellite time step (e.g., Zhang et al, 2022).

201   Moreover, estimating the cloud susceptibility over a confined space also help to constrain the meteorological

202   impacts on AIE, with the assumption of a homogeneous meteorological condition within this spatial scale. Next,

203   susceptibilities are calculated using the 0.25° smoothed data if the number of data points within the $1° \times 1°$ box

204   exceeds six (from a maximum of 16 data points). It is important to note that when computing the $0.25° \times 0.25°$

205   averaged cloud properties, only data from cloudy pixels are used to ensure that the estimated susceptibility is not

206   weighted by CF or impacted by satellite artifacts. Lastly, due to the minimal spatial variability of cloud

207   susceptibility in the study region, the 1° cloud susceptibility is averaged over the study region (33-43°N, 23-33°W)

208   to characterize the daytime variation of AIE. Additionally, results and conclusions of this study are not sensitive to

209   the size of the box calculating the cloud susceptibility (e.g., over a $0.8° \times 0.8°$ box or over a $1.5° \times 1.5°$ box, not

210   shown).

211   Because of the nonlinear relationships between LWP and N_d, the LWP susceptibility is defined as the slope

212   in logarithmic scale, that is: $dln(LWP)/dln(N_d)$ (e.g., Gryspeerdt et al. 2019). The albedo susceptibility is

213   estimated as the slope between α_c and $ln\ (N_d)$, equivalent to $d\alpha_c/dln(N_d)$ (e.g., Painemal 2018). Lastly, the CF

214   susceptibility is estimated as $dCF/dln(N_d)$. The mean CF is defined as the fraction of cloudy pixels excluding

215   cloud edge to the sum of cloudy and clear pixels within each $0.25° \times 0.25°$ box. Due to the highly variable nature of

216   CF, the variability in the 0.25° CF could arise from quantifying edges or centers of the same cloud layer rather than

217   N_d perturbations. To assess the potential influence of cloud morphology on the retrieved CF susceptibility, we

218   excluded any $1° \times 1°$ scene meeting the following three criteria: 1) the difference between the maximum and

219   minimum 0.25° CF greater than 0.9, 2) the variation in the 0.25° N_d less than $60\ cm^{-3}$, and 3) the 0.25° CF in the

220    $1° \times 1°$ box sample the same cloud. The 0.9 and $60\ cm^{-3}$ thresholds represent ~45% of the data. With the three

221   thresholds combined, a total of 17,000 scenes were removed, which accounts for ~24% of the total samples.

7

222 Removing these scenes does not change the conclusions of CF susceptibility in this study (not shown), which

223 demonstrates that cloud morphology, has minimal impact on the retrieved CF susceptibility. Furthermore, as we

224 removed N_d retrievals at cloud edge where N_d likely suffers large uncertainties, cloudy pixels at cloud edge are set

225 as clear for consistency in the calculation of the CF susceptibility. Removing the cloud edge decreases the four-

226 month mean CF for warm boundary layer clouds from 21.6% to 19.0%.

227   The susceptibility of the shortwave radiative fluxes to N_d (F_0) is estimated as the sensitivity of the TOA

228 shortwave upward radiative flux (SW_{TOA}^{up}) to N_d perturbations (e.g., Chen et al. 2014; Painemal 2018; Zhang et al.

229 2022). The mean SW_{TOA}^{up} over a $1° \times 1°$ grid box is estimated using Eq. (2), with the assumption that the clear-sky

230 albedo over the ocean is small compared to the cloud albedo:

231
$$\overline{SW_{TOA}^{up}} = \overline{SW_{TOA}^{dn}} \cdot \overline{\alpha_c} \cdot \overline{CF}, \tag{2}$$

232 where SW_{TOA}^{dn} is the grid-box mean TOA shortwave downward radiative flux, which is estimated based on the

233 latitude, longitude, date, and overpass time of each pixel, α_c and CF are the grid-box mean values. Then, F_0 is

234 estimated using the calculated α_c and CF susceptibilities, and the $1° \times 1°$ grid-box mean cloud properties as shown

235 in the equation below:

236
$$F_0 = -\frac{dSW_{TOA}^{up}}{dln(N_d)} = -\overline{SW_{TOA}^{dn}} \cdot \left(\frac{d\alpha_c}{dln(N_d)} \cdot \overline{CF} + \frac{dCF}{dln(N_d)} \cdot \overline{\alpha_c}\right). \tag{3}$$

237 F_0 is in the unit of $W \ m^{-2} \ ln \ (N_d)^{-1}$, and a positive value indicates a decrease in the SW_{TOA}^{up}, which is a *warming*

238 effect at the surface.

239   To minimize uncertainties in the linear regression for the estimated susceptibility, we analyze regressions

240 that exhibited a goodness of fit exceeding the 95% confidence interval (i.e., $\chi^2 < \chi^2_{0.95,c}$), and an absolute

241 correlation coefficient greater than 0.2 (e.g., Painemal, 2018; Zhang et al., 2022). There is a total of ~115,000

242 samples of the 1° cloud susceptibilities in this study, applying the goodness of fit thresholds result in exclusions of ~

243 33,000- 43,000 samples for different susceptibilities, which are ~28-37% of the data. Sensitivity test shows that

244 including cases that fail the goodness of fit test will not change the results and conclusions of this study (not shown).

245 Specifically, including these cases decrease the magnitude of cloud susceptibilities for all three cloud states, but the

246 signs of cloud responses to N_d perturbations remain consistent.

247   Since precipitating and non-precipitating clouds exhibit distinct responses to aerosol perturbations due to

248 the effect of precipitation suppression and the wet-scavenging feedback, it is critical to distinguish between these

249 two cloud states when estimating AIE. Previous studies have utilized various methods based on the effective radius

250 threshold (e.g., Gryspeerdt et al., 2019, Toll et al., 2019; Zhang et al., 2022) and the rain rate threshold (e.g., Duong

251 et al., 2011; Terai et al., 2015) from satellite retrievals. In our study, we validate these two methods using the

252 precipitating mask estimated from ground-based observations with a radar reflectivity threshold together with the

253 lidar-defined cloud base at the ARM ENA site (e.g., Wu et al., 2020). The thresholds of $r_e >12 \ \mu m$ and $r_e >15 \ \mu m$

254 yield hit rates of 0.79 and 0.73, respectively. However, the false alarm rate is higher for $r_e >12 \ \mu m$ (0.21) compared

255 to $r_e >15 \ \mu m$ (0.1). Rain rate is computed using the empirical relationships derived from ground-based

256 measurements in Comstock et al. (2004) as $R = 0.0156 \ \left(LWP/N_d\right)^{1.75}$. Using a threshold of R>0.05 mm/h results

257 in a hit rate of 0.65. Consequently, we use the $r_e >15 \ \mu m$ threshold to define precipitating clouds in this study.

258   To investigate the dependences of cloud susceptibility on previous cloud states and quantify the influence
259   of cloud memory on the estimated cloud susceptibility, we track the historical cloud state over a $1° \times 1°$ grid box for
260   a two-hour period. During the summer in the study region, low wind conditions prevail in the boundary layer, with
261   the mean wind speed being less than 10 m/s for 85% of the time and less than 7 m/s for 60% of the time. Therefore,
262   in most cases, less than half of the clouds exit the grid box within the two hours, allowing us to track the previous
263   cloud state within the same grid box (i.e., from an Eulerian perspective). The influence of cloud memory is assessed
264   by comparing the cloud susceptibilities of clouds that undergo a transition in cloud state with those that do not
265   experience such a transition. Section 3.4 provides more details and discussion on the sensitivity of tracking time and
266   the influence of advection on our classification.

267   **3. Results**

268   **3.1 General cloud conditions and mean cloud responses to N_d perturbations**

269   In the ENA region, characterized by dominant Bermuda High with its prevailing ridge and zonal synoptic
270   pattern (Mechem et al., 2018), the summer season gives rise to the annual peak in boundary layer cloud coverage
271   The monthly mean low-level CF retrieved from Meteosat-11 reaches its maximum of 35% in July, compared to an
272   annual mean of 17% during the four-year study period. This region represents a typical clean marine condition,
273   situated far from continental influences, which results in a consistently low N_d compared to polluted marine regions,
274   such as the northeastern (NE) Pacific near California or the northwestern Atlantic near the Gulf of Maine. In July,
275   the mean N_d over the ENA region is 65 cm^{-3} with the lower 5th and upper 95th percentile of 15 and 160 cm^{-3},
276   respectively. The retrieved N_d values in this study closely align with in-situ measurements from the Aerosol and
277   Cloud Experiments in Eastern North Atlantic (ACE-ENA) field campaign. For instance, the in-situ measured N_d in
278   July 2017 varied from 25 to 150 cm^{-3}, with a mean value of 65 cm^{-3} (e.g., Yeom et al., 2021; Zhang et al., 2021).
279   Moreover, our satellite retrieved N_d exhibits good agreement with retrievals based on ground-based observations at
280   the ARM ENA site (e.g., Dong et al., 2014; Wu et al., 2020) and the MOderate resolution Imaging
281   Spectroradiometer (MODIS, e.g., Bennartz 2007; Bennartz and Rausch 2017).
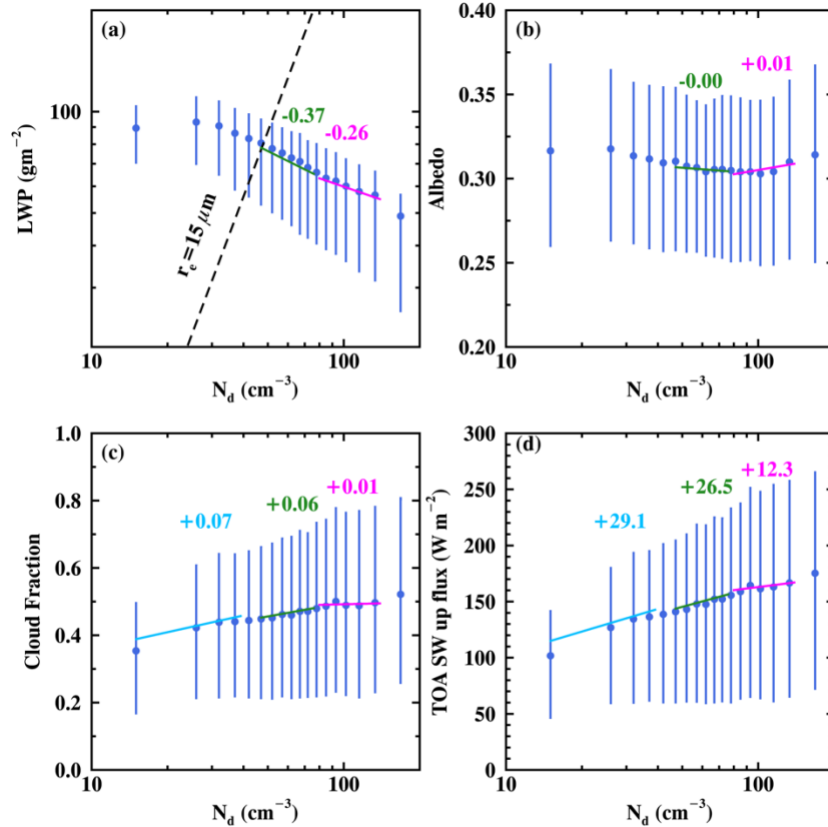
Figure 1. Relationships between N_d and cloud properties: (a) cloud LWP, (b) cloud albedo, (c) cloud fraction, and (d) TOA shortwave upward radiative flux. The dots represent the mean values, while the whiskers indicate the upper and lower 25th percentile. In (a), the dashed line denotes $r_e = 15\ \mu m$, serving as an indicator of precipitation occurrence, with precipitating clouds located to the left of the line. Blue, green, and magenta lines in panels (a)-(d) represent the regression slopes of the mean cloud properties, and the mean $ln(N_d)$, for $N_d < 40\ cm^{-3}$, N_d between 40 and 80 cm^{-3}, and $N_d > 80\ cm^{-3}$, respectively.

Previous studies have demonstrated that clouds exhibit diverse responses to aerosol perturbations under clean and polluted conditions (e.g., Fan et al. 2016; Mülmenstädt and Feingold, 2018). Figure 1 shows the relationships between the climate mean cloud properties, derived from the pixel-level SEVIRI cloud products, and averaged to the 1° × 1° resolution, as a function of the 1° × 1° mean N_d values. To quantify these responses, cloud susceptibility is estimated as the slope of the mean cloud variable changes across N_d bins. In pristine conditions (N_d < 40 cm^{-3}, ~28% of data), clouds predominantly precipitate (r_e >15 μm, Fig.1a). The mean cloud LWP features a slight increase followed by a decrease with increasing N_d. This result departs from the precipitation suppression hypothesis, in which LWP typically increases. The absence of a precipitation suppression signal is likely attributed to the relatively modest precipitation that occurs in this region during summer (e.g., Wu et al., 2020; Zheng and Miller, 2022), resulting in a minimal precipitation suppression effect and a dominant entrainment drying effect. In terms of α_c, the potential decrease in α_c attributed to a LWP reduction offsets the potential increases in α_c caused by the Twomey effect, resulting in a net zero change in mean α_c for clouds with $N_d < 40\ cm^{-3}$ (Fig.1b). Furthermore, the majority of precipitating clouds are broken, with a mean CF that increases with N_d from 0.35 to 0.45 (Fig.1c). Consequently, the mean SW_{TOA}^{up} flux increases from 100 to 140 $W\ m^{-2}$ as N_d increases from 10 to 40 cm^{-3}. This

10

303   increase in CF for precipitating clouds aligns with previous study over the north Atlantic region across all seasons

304   (e.g., Gryspeerdt et al., 2016). In summary, despite the slight decrease in mean LWP with increasing N_d for

305   precipitating clouds, the mean cloud albedo remains relatively constant, while the mean CF increases, resulting in an

306   overall increase in the TOA reflected shortwave flux.

307   Under relatively polluted conditions with $N_d > 40\ cm^{-3}$ (~72% of data), the mean LWP shows a

308   decreasing trend with N_d. For N_d values between 40-80 cm^{-3}, the ln(LWP)- $ln(N_d)$ slope is -0.37, while for N_d

309   exceeding 80 cm^{-3}, the slope reaches -0.26 (green and magenta lines in Fig.1a). This negative adjustment of LWP

310   for non-precipitating clouds is consistent with the sedimentation-evaporation-entrainment feedback, as well as with

311   previous studies of stratocumulus clouds in other regions (e.g., Gryspeerdt et al., 2019; Zhang et al., 2022). The

312   mean α_c remains nearly constant within the N_d range of 40-80 cm^{-3} (Fig.1b). As LWP decreases at a slower rate

313   for $N_d >80\ cm^{-3}$, the Twomey effect becomes more dominant and leads to a slight increase in α_c with a slope of

314   0.01 (magenta line in Fig.1b). For non-precipitating clouds, the mean CF slightly increases with increasing N_d with

315   a CF susceptibility of 0.06 and 0.01 (green and magenta lines in Fig.1c). As a result, the SW_{TOA}^{up} flux exhibits a

316   weaker susceptibility compared to precipitating clouds (Fig.1d).

317   **3.2 Daytime mean cloud susceptibilities in the LWP-N_d space**

318   One limitation of the relationships derived from the mean cloud properties with sorted N_d is the

319   confounding effect from meteorological impacts on cloud properties and cloud susceptibilities. As a comparison,

320   Fig.2 shows the mean cloud susceptibility estimated within each half-hourly snapshot's $1° \times 1°$ grid box and

321   averaged in the LWP-N_d parameter space. There are around 72,000-82,000 samples of the 1° cloud susceptibilities

322   in this study. The number of samples for different cloud susceptibilities are slightly different due to the goodness of

323   fit test for each regression. We calculate the mean susceptibilities for LWP-N_d bins with more than 100 cloud

324   susceptibility samples. Blank bins in Fig.2 are bins with less than 100 samples. Figure 2e shows the occurrence

325   frequency of samples for the LWP susceptibility in Fig.2a.

326   With the assumption that the meteorological condition is homogeneous in each grid box, the estimated

327   cloud susceptibilities exhibit much stronger relationships for all cloud variables compared to the climatological

328   mean adjustment rates shown in Fig.1. The disparities between the two methods suggest that meteorological

329   confounders tend to obscure the signal of the AIE over the ENA region. Moreover, the cloud responses for both

330   precipitating and non-precipitating clouds exhibit consistent signs between the half-hourly (Fig.2) and

331   climatological-mean approaches (Fig.1). This consistency is likely attributed to the confined domain (a $10° \times 10°$)

332   and the focus on July in this study, which limit the spatial and temporal covariability between cloud properties and

333   N_d. This consistency also demonstrates that the overall cloud responses to N_d perturbations primarily depend on

334   cloud states (e.g., precipitating conditions and cloud thickness).

335   The dependence of cloud response on cloud state is illustrated in Fig.2. We define three cloud states*: (1)*

336   *the precipitating clouds (r_e>15 μm),(2) the non-precipitating thick clouds (r_e<15 μm, LWP > 75 gm^{-2}),* and (3)

337   *the non-precipitating thin clouds (r_e<15 μm, LWP < 75 gm^{-2}),* similar to the definition in Zhang et al. (2022).
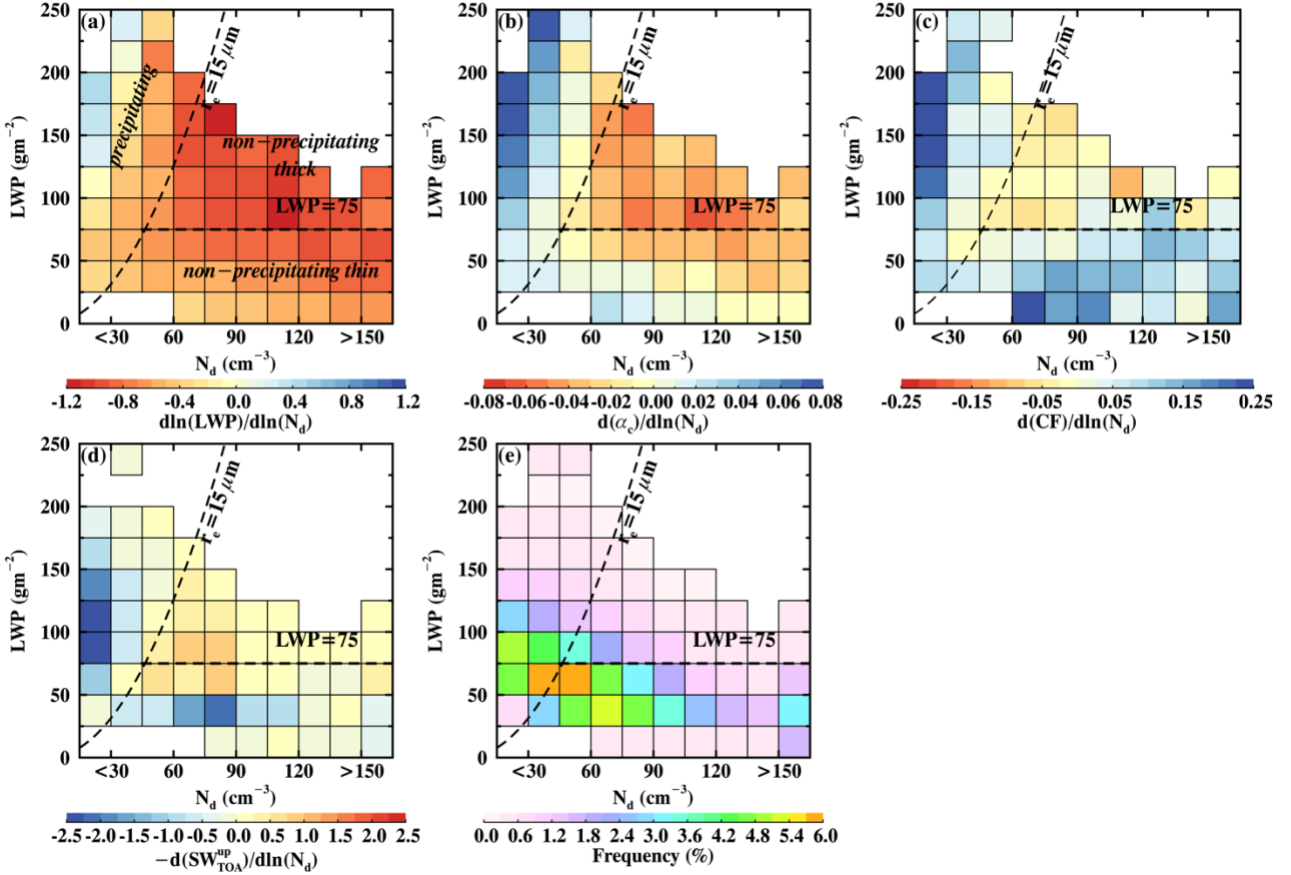
Figure 2. Mean cloud susceptibilities for different N_d and LWP bins during the daytime. (a) cloud LWP susceptibility ($dln(LWP)/dln(N_d)$), (b) cloud albedo susceptibility ($d\alpha_c/dln(N_d)$), (c) cloud fraction susceptibility ($dCF/dln(N_d)$), (d) cloud shortwave susceptibility ($-dSW_{TOA}^{up}/dln(N_d)$) weighted by the frequency of occurrence of samples of each bin, and (e) frequency of occurrence of samples in each bin. The dashed lines in (a)-(e) indicate $r_e =15 \mu m$ and LWP= 75 gm^{-2}, as thresholds for precipitation (precipitating clouds located to the left of the line) and thick clouds (with LWP > 75 gm^{-2}). The defined three clouds states are noted in (a).

a. Precipitating clouds

Among warm boundary layer clouds, precipitating clouds are the dominant cloud state in July over the study region, with a total frequency of occurrence of 46% (Fig.2e). The increase in cloud LWP with increasing N_d is observed primarily in heavily precipitating thick clouds with $N_d < 30 cm^{-3}$ and LWP > 125 gm^{-2} (Fig.2a). However, these clouds occur relatively infrequently at ENA, accounting for only 2% of the total warm boundary cloud population (Fig.2e). In contrast, most of the precipitating clouds at ENA are lightly precipitating with $15 < r_e < 20 \mu m$ (Fig.2e and Fig.S2c) and they exhibit a slight decrease of LWP with N_d (Fig.2a). The mean LWP susceptibility for lightly precipitating clouds ranges from -0.5 to -0.2 for different bins, with a mean value of -0.4. The standard deviations of LWP susceptibility in different LWP-N_d bins vary between 0.4 to 1.2, while the LWP susceptibilities for precipitating clouds are significantly different than other two cloud states at a 95% confidence level. The slight decrease in LWP for lightly precipitating clouds aligns with previous findings over the Pacific, Atlantic, and global oceans for marine stratocumulus (e.g., Fig S4 in Zhang and Feingold, 2023).

357   The contrasting response of LWP to N_d perturbations for lightly and heavily precipitating clouds can be

358   attributed to the interplay of two competing processes: the depletion of LWP caused by the sedimentation-

359   evaporation-entrainment feedback and the accumulation of LWP resulting from the precipitation suppression

360   feedback. Heavily precipitating clouds are predominantly overcast with a mean CF of 0.65 (Fig.S2a) and a mean r_e

361   of 25 μm (Fig.S2c). Precipitation acts to stabilize the boundary layer, remove water from cloud top, and reduce the

362   entrainment rate (Sandu et al., 2007, 2008). Therefore, heavily precipitating clouds exhibit smaller entrainment rate

363   than non-precipitating clouds with similar LWP. The increase of LWP from precipitating suppression feedback

364   outweighs the decrease of LWP from entrainment feedback and results in a net increase in LWP (e.g., Chen et al.,

365   2014; Toll et al., 2019). In lightly precipitating clouds, however, the suppression effect of drizzle on the entrainment

366   rate is minimal. Therefore, the decrease in LWP from entrainment overpowers the increases in LWP from

367   precipitating suppression, leading to a net decrease in LWP with increasing N_d (e.g., Xue and Feingold, 2006).

368   Precipitating clouds generally exhibit brighter cloud albedo with increasing N_d as a result of the weak

369   negative and positive LWP adjustment, particularly in heavily precipitating clouds (Fig.2b). For lightly precipitating

370   clouds, α_c susceptibilities range from -0.04 to 0.07 $ln(N_d)^{-1}$, with a mean of 0.02 $ln(N_d)^{-1}$. The suppression of

371   precipitation by N_d also lead to a significant increase in CF for heavily precipitating clouds, with slopes greater than

372   0.25 $ln(N_d)^{-1}$. For most of the lightly precipitating clouds, the mean CF exhibits small variation with N_d

373   perturbations, with CF susceptibilities ranging between ±0.025 $ln(N_d)^{-1}$ (Fig.2c). The standard deviation of the

374    $1°$ α_c and CF susceptibilities for different precipitating bins ranges between 0.05-0.15 and 0.3-0.6, respectively. The

375   α_c and CF susceptibilities for precipitating clouds are significantly different than other two cloud states at a 95%

376   confidence level. Considering the combined effects of increased α_c and CF, the mean radiative response for

377   precipitating clouds amounts to -13 W $m^{-2} ln(N_d)^{-1}$, which is a cumulative shortwave susceptibility of bins

378   classified as precipitating clouds in Fig.2d, weighted by their frequency of occurrence. The contributions from CF

379   and α_c effects are -9.5 and -3.5 W m^{-2} $ln(N_d)^{-1}$, respectively (Eq. 3).

380   *b.   Non-precipitating thick clouds*

381   Non-precipitating thick clouds are less frequent, the total frequency of occurrence is 10% (Fig.2e). Their

382   cloud LWP responses to N_d perturbations differ from that of precipitating clouds. The LWP susceptibility for non-

383   precipitating thick clouds is the most negative among the three cloud states, and it reaches a minimum value of -1.2

384   at the high-LWP and high-N_d ends (Fig.2a). As LWP and N_d decrease, the LWP susceptibility gradually increases

385   from -1.2 to -0.6. This negative susceptibility is likely explained by the evaporation enhancement associated with

386   smaller droplets at high N_d values (e.g., Xue and Feingold, 2006; Small et al., 2009), which works in concert with an

387   entrainment strengthening expected in clouds with large LWP (e.g., Sandu et al., 2008, Williams and Igel, 2021).

388   The mean LWP susceptibility for non-precipitating thick clouds is -0.94. Consistent with the negative LWP

389   susceptibility, non-precipitating thick clouds become less reflective with increasing N_d for all N_d bins with LWP $>$

390   75 gm^{-2} (Fig.2b). The mean α_c susceptibility is -0.04 $ln(N_d)^{-1}$. Due to the enhanced entrainment and

391   evaporation, the mean CF mostly decreases with increasing N_d, with the mean CF susceptibilities ranging from -0.1

392   to $+0.04$ $ln(N_d)^{-1}$ (Fig.2c). Considering the decrease in both α_c and CF, non-precipitating thick clouds exhibit a

13

393　warming effect at the surface, the mean radiative response is $+4.4 \ W \ m^{-2} \ ln(N_d)^{-1}$ (Fig.2d), with contributions

394　from the albedo effect and the CF effect of 2.9 and $1.5 \ W \ m^{-2} \ ln(N_d)^{-1}$, respectively.

395　*c.　Non-precipitating thin clouds*

396　　　　Non-precipitating thin clouds are more common than thick clouds during summer, with a total frequency of

397　occurrence of 44% (Fig.2e). Compared to non-precipitating thick clouds, they exhibit consistent negative but

398　slightly weaker LWP responses to N_d perturbations. The mean LWP susceptibilities range from -0.9 to -0.4 in

399　different LWP-N_d bins with a mean of -0.7 (Fig.2a). Similar to non-precipitating thick clouds, non-precipitating

400　thin clouds mostly become darker with increasing N_d. Interestingly, with largely decreased LWP, the mean CF

401　mostly increase for all N_d conditions, the CF susceptibilities range from $+0.02$ to $+0.25 \ ln(N_d)^{-1}$ (Fig.2c). The

402　sedimentation- evaporation-entrainment feedback alone cannot explain the opposite signs in in LWP and CF

403　susceptibilities for non-precipitating thin clouds. A possible explanation for the increased CF is that the enhanced

404　cloud top radiative cooling rate from aerosol perturbations help to mix the boundary layer, facilitate moisture

405　transport from the ocean surface to cloud, and therefore favor new cloud formation and extend cloud lifetime (e.g.,

406　Christensen et al. 2020). This hypothesis is consistent with and supported by the relative low CF for these clouds

407　(Fig.S2a) and the diurnal variation in LWP susceptibility for non-precipitating thin clouds, which will be discussed

408　in the next section. The opposite signs of LWP and CF susceptibilities indicate that the AIE might redistribute cloud

409　water horizontally and make the thin clouds thinner and wider. The CF radiative effect from increased CF

410　dominates the albedo effect from darker clouds and lead a net cooling at the surface. The mean radiative response is

411　$-5.2 \ W \ m^{-2} ln(N_d)^{-1}$, with CF and albedo contributions of -8.3 and $+3.1 \ W \ m^{-2} ln(N_d)^{-1}$, respectively (Fig.2d).

412　　　　To sum up, the magnitudes and signs of the responses of cloud LWP, α_c, and CF to N_d perturbations

413　primarily depend on the cloud states. Precipitating clouds mostly become thinner and brighter with increasing N_d,

414　accompanied by a slight increase in CF. An increase in LWP with increasing N_d is observed only for heavily

415　precipitating clouds with $N_d < 30 \ cm^{-3}$ and LWP $> 125 \ gm^{-2}$. Non-precipitating thick clouds become thinner, less

416　reflective, and decrease in cloudiness with N_d perturbations. On the other hand, non-precipitating thin clouds

417　become thinner and less reflective, but their cloudiness increase as N_d increases. Given the dependence of AIE on

418　cloud state, we will apply the cloud state classification in the following two sections with the goal of facilitating a

419　process-level understanding of cloud responses and the daytime variation in cloud susceptibilities.

420　**3.3 Daytime variation of cloud susceptibility**

421　　　　As discussed in the introduction, warm boundary layer clouds exhibit a distinct diurnal cycle in both cloud

422　properties and frequency of occurrence of cloud states during summer. In this section, we investigate the daytime

423　variation of cloud susceptibility from 9 to 18 local standard time (LST) using the half-hourly Meteosat-11 retrievals.

424　The domain mean daytime variation of cloud susceptibility is estimated from each half-hourly time step within each

425　$1° \times 1°$ box and then averaged over the study domain (33-43°N, 23-33°W) during the four months. In the study

426　domain, there is little spatial variability in cloud susceptibilities and the diurnal cycle of the cloud susceptibility for

427　the $1° \times 1°$ box at the ARM ENA site agree well with the domain mean pattern (not shown). Furthermore, diurnal

428　cycle of the cloud microphysical properties (e.g., r_e, τ, LWP, N_d) show little difference between the domain mean

14

429 value or that averaged over the 1° × 1° box at the ARM ENA site. The cloud microphysics retrievals from

430 Meteosat-11 agree well with retrievals based on ground-based radar and lidar observations in the daytime variation

431 (not shown). Therefore, the ARM ENA site at the Azores archipelago can represent the cloud properties and the AIE

432 for warm boundary layer clouds over the study region.
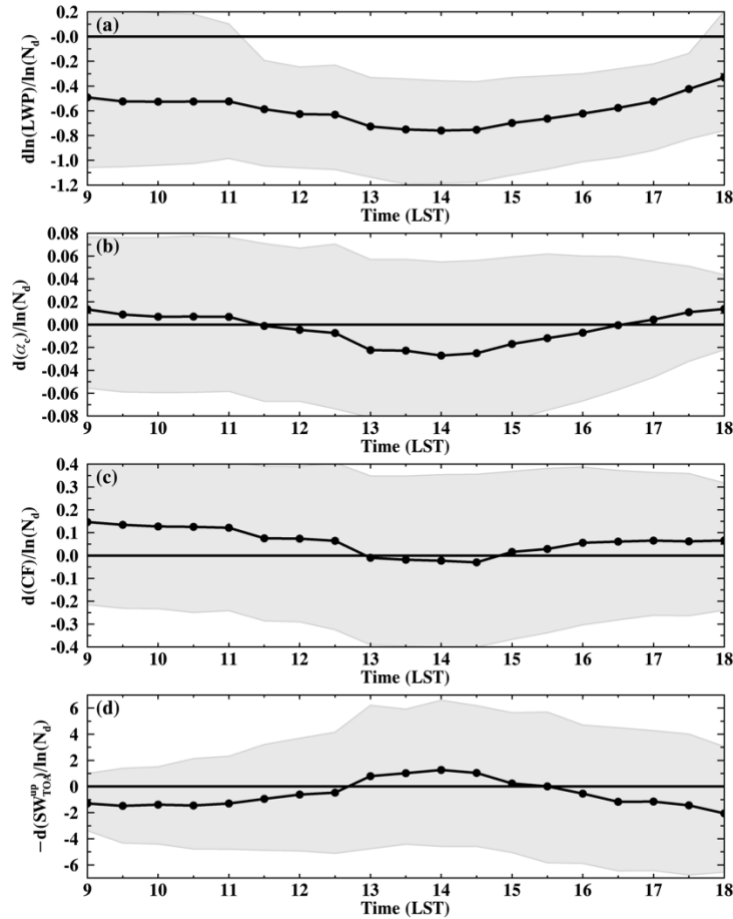
433
434 Figure 3. Daytime variation of cloud susceptibilities. (a) cloud LWP susceptibility ($dln(LWP)/dln(N_d)$), (b) cloud
435 albedo susceptibility ($d\alpha_c/dln(N_d)$), (c) cloud fraction susceptibility ($dCF/dln(N_d)$), and (d) cloud shortwave
436 susceptibility ($-dSW_{TOA}^{up}/dln(N_d)$). The shaded areas represent the lower and upper 25th percentile of the cloud
437 susceptibilities for each time step and the solid lines with dots represent the mean values.

438   Warm boundary layer clouds witness distinct and significant daytime variations in cloud susceptibilities

439 (Fig.3). For example, the mean LWP susceptibility exhibits a magnitude of change of 0.4 from morning to evening,

440 which corresponds to approximately 30-40% of the overall variability in LWP susceptibility (Fig.3a). Similarly, the

441 α_c and CF susceptibility undergo magnitude of changes of approximately 20-30% compared to the overall

442 variability (Figs. 3b and c). The high variability in cloud susceptibility highlights the complex synoptic,

443 meteorological and cloud conditions as well as the interplay between them in the ENA region. Nevertheless, the

444 daytime variation of cloud susceptibility is statistically significant at a 95% confidence level based on a student's t-

445 test. Interestingly, all three cloud variables exhibit a "U-shaped" diurnal cycle in cloud susceptibilities with less

446 negative/more positive values in the morning and evening and more negative values at noon. Additionally, the α_c

15

447 and CF susceptibilities switch signs from positive in the morning to negative at noon, and then become positive

448 again in the evening. The switch in sign for albedo susceptibility is statistically significant at a 95% confidence

449 level, while the switch in sign for CF susceptibility is not statistically significant. As both α_c and CF increase with

450 increasing N_d in the morning, AIE has a cooling effect at the surface and the estimated shortwave susceptibility is

451 $-1.4\ W\ m^{-2}\ ln(N_d)^{-1}$. During 13-15 LST, the shortwave susceptibility switches sign to a warming effect of

452 $+1.2\ W\ m^{-2}\ ln(N_d)^{-1}$ (Fig.3d).

453   Given the pronounced daytime variation of cloud susceptibility, *how can we explain this distinct daytime*

454 *variation, and which state of cloud contributes most to the daytime variation?* One possible explanation is the

455 increased occurrence of precipitating clouds in the morning and evening during summer (Remillard et al, 2012),

456 which increase cloud susceptibility, as depicted in Fig.2. To investigate this hypothesis and quantify the impacts of

457 different cloud states on the variabilities of cloud susceptibilities, we examined the daytime variation of cloud

458 susceptibility, along with the daytime shift in occurrence frequency for each cloud state.

459 **3.4 Daytime variation of cloud susceptibility for different cloud states**

460 **3.4.1 Non-precipitating thin clouds**

461   Non-precipitating clouds mainly consist of thin clouds, with a daytime mean occurrence of 44% (Fig.4a).

462 The highest occurrence is observed around noon, which is consistent with ground-based radar reflectivity

463 measurement at the ENA site (Remillard et al, 2012). Furthermore, as seen in Fig.4, not only the frequency of cloud

464 occurrence, but also the susceptibilities of LWP, α_c, and CF show distinct daytime fluctuations. For example, the

465 mean LWP susceptibility decreases from -0.4 to -0.9, and the mean α_c susceptibility decreases from 0.02 to -0.04

466 $ln(N_d)^{-1}$ from morning to noon, followed by increases in both LWP and α_c susceptibilities in the afternoon. The

467 CF susceptibility is highly positive in the morning and decreases to near zero after 13 LST. In addition, cloud

468 susceptibility for thin clouds in the morning is statistically significantly different from that at noon and in the

469 evening at a 95% confidence level.

470
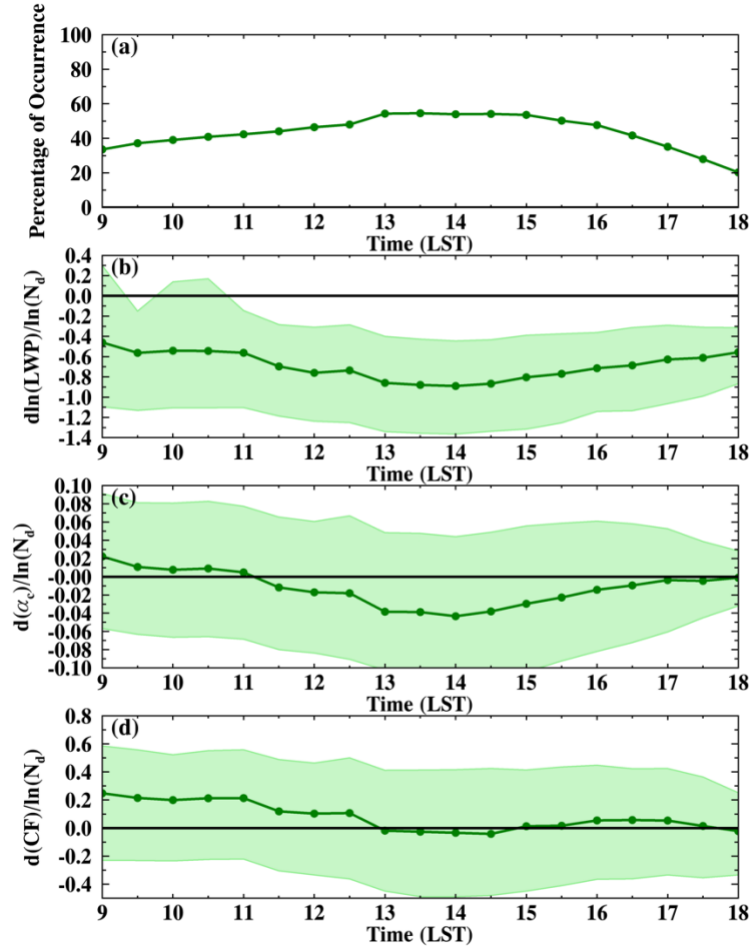
Figure 4. Daytime variation of (a) percentage of occurrence of non-precipitating thin clouds to warm boundary layer clouds, (b) cloud LWP susceptibility ($dln(LWP)/dln(N_d)$), (c) cloud albedo susceptibility ($d\alpha_c/dln(N_d)$), and (d) cloud fraction susceptibility ($dCF/dln(N_d)$) for non-precipitating thin clouds. The shaded areas represent the lower and upper 25th percentile of the cloud susceptibilities for each time step and the solid lines with dots represent the mean values.

To explain the decrease of cloud susceptibility of non-precipitating thin clouds from morning to noon, we test two hypotheses (H1 and H2 in Table 1). Hypothesis H2 is related to the dissipation of thin clouds during this period, which is caused by a decreased LWP due to increased solar radiation. During the dissipation, both LWP and r_e decrease. As r_e is raised to the power of $-\frac{5}{2}$ in Eq. (1) compared to τ being raised only to the power of $\frac{1}{2}$, the decreases of LWP and r_e could still result in an increase in the retrieved N_d. Consequently, a LWP decrease and N_d increase lead to a decrease in LWP susceptibility during the dissipation (Gryspeerdt et al., 2019). To examine this hypothesis (H2), non-precipitating thin clouds are classified as: growing, dissipating, or constant based on the changes in the mean CF, cloud susceptibilities for the three groups are shown in Fig.S3. More specifically, we calculate the change in the mean CF within a 30-minute window for each fixed $1° \times 1°$ box. If the mean CF increase (decrease) more than 10%, clouds are classified as growing (dissipating). If the change in CF is less than 10%, clouds are classified as constant. Similar results are obtained using classification methods based on different CF thresholds (e.g., from 10% to 30%), and during different time windows from 30-minutes to two hours (not shown).

17

Table 1. List of hypotheses and associated explanations for the daytime variation of LWP and CF susceptibilities for different cloud states.

	Cloud state	Hypotheses:	
Daytime evolution of LWP susceptibility	Non-precipitating thin clouds	H1*:	Non-precipitating thick clouds transition to thin clouds from morning to noon, which leads to a daily minimum LWP susceptibility at noon.
		H2*:	Cannot explain. Clouds that are growing or dissipating have similar LWP susceptibilities as clouds with constant CF.
	Non-precipitating thick clouds	H1:	Thin clouds develop to thick clouds from noon to evening, which leads to an increase in LWP susceptibility.
		H2:	Cannot explain.
	Precipitating clouds	H1:	Non-precipitating thin clouds transition to precipitating clouds in the afternoon, which leads to a decrease in LWP susceptibility.
		H2:	Cannot explain.
Daytime evolution of CF susceptibility	Non-precipitating thin clouds	H1:	Thick clouds transitioned to thin clouds from morning to noon, leading to a decrease in CF susceptibility
		H2:	Cannot explain.
	Non-precipitating thick clouds	H1:	Cannot explain.
		H2:	Cannot explain.
		H3*:	Mostly overcast clouds in the morning and evening. CF of overcast clouds is less sensitive to N_d perturbations.
	Precipitating clouds	H1:	Thin clouds transition to precipitating clouds in the afternoon, and lead to a decrease in CF susceptibility
		H2:	Cannot explain.

*H1: LWP and CF responses to N_d perturbations slower than the transition of cloud state.
*H2: Dissipation or development of clouds.
*H3: Changes in cloud morphology.

As seen in Fig. S3b, the LWP susceptibilities for non-precipitating thin clouds in the growing or dissipating stages are similar or less negative than clouds that remain constant in CF, which contradicts the hypothesis H2. Additionally, the occurrence of dissipating and developing thin clouds remain relatively constant throughout the day (Fig.S3a), which differs from our hypothesis that thin clouds dissipate in the morning. Therefore, the decrease in LWP susceptibility in the morning is *unlikely* to be attributed to the dissipation or development of thin clouds. Yet, due to the observational limitation on estimating the mixing process from satellite retrievals, further investigation is needed to quantify the impact of cloud dissipation on the N_d-LWP relationship.

Besides the change in CF, dissipation/development of clouds can be defined by change in LWP. However, as our definition of thin and thick clouds use LWP thresholds, results based on change in LWP are similar to results shown in Fig.5, but with weaker signal (not shown). This indicates that classification of precipitating verses non-precipitating clouds is necessary in distinguishing cloud responses to N_d perturbations than merely using the LWP threshold.

506   Hypothesis H1 is related to the response time of cloud LWP and CF to N_d perturbations. Both numerical

507   models and observations have shown that the influence of aerosols on cloud LWP, achieved through adjusting the

508   entrainment rate, may take four hours to become apparent and up to 20 hours to reach an equilibrium (Glassmeier et

509   al. 2021; Gryspeerdt et al., 2021). Similarly, CF increases gradually from increasing aerosols and may take

510   approximately three to four hours to reach its maximum effect after the initial perturbation (Gryspeerdt et al., 2021).

511   Therefore, we hypothesize that if clouds change state during the adjustment time, clouds may still retain the

512   "memory" of their susceptibilities from the previous state. The possible physical processes and mechanisms for this

513   hypothesis is that the LWP susceptibility is mainly driven by cloud top evaporation and entrainment rate. The

514   positive feedback among entrainment, evaporative cooling, long-wave radiative cooling, and mixing from cloud top

515   form a positive feedback loop and set up an environment conductive to enhanced entrainment and evaporation.

516   These feedback and environment will not change immediately even when the cloud LWP decrease and cloud

517   transition to a thin state or vice versa. With the diurnal variation in cloud properties and transition in cloud state it

518   leads to a diurnal evolution in cloud susceptibility.

519   To quantify the dependence of current cloud susceptibility on previous cloud states, we track the cloud state

520   for each $1° \times 1°$ box backward in time for two hours and classify the non-precipitating thin clouds into three groups

521   (Fig.5): (1) thin clouds that are currently classified as thin clouds and didn't change states in the past two hours (thin

522    $\rightarrow$ thin), (2) thin clouds that evolved from precipitating clouds (rain $\rightarrow$ thin), and (3) thin clouds that decayed from

523   non-precipitating thick clouds (thick $\rightarrow$ thin). This backward tracking classification is applied at each time step. As

524   shown in Fig.5a, at 9 LST, ~50% of the non-precipitating thin clouds originate from thick clouds in previous hours.

525   The transition from thick to thin clouds is likely caused by the increased solar radiation after sunrise, leading to

526   cloud turbulent decoupling from the ocean surface and a decrease in cloud LWP. In the evening, on the other hand,

527   around 80% of the thin clouds are thin clouds in previous hours. In addition, less than 20% of the non-precipitating

528   thin clouds transition from precipitating clouds.

529   In consistent with our hypothesis, non-precipitating thin clouds that are previously thick have significantly

530   more negative LWP and α_c susceptibilities than thin clouds that are previously thin or precipitating (Figs. 5b and c).

531   The differences between the two categories are most pronounced from late morning to early afternoon and less

532   pronounced in the early morning and evening. Such pattern is likely attributed to the daytime evolution of marine

533   boundary layer and cloud coupling state. For example, in the early morning (e.g., 9-10 LST), even with higher

534   frequency of occurrence of thick clouds transitioning to thin clouds, the LWP susceptibility for the thick-to-thin

535   category is less negative compared to later time (dashed line with diamond symbols in Figs 5a, b). This is attributed

536   to the less negative LWP susceptibility for non-precipitating thick clouds in earlier time (e.g., 7-9 LST, not shown),

537   in connection with a well-mixed boundary layer able to transport moisture from the ocean to the cloud, which

538   compensates the moisture loss from aerosol-enhanced entrainment (e.g., Sandu et al., 2008), so that both thick and

539   thin clouds exhibit less negative LWP susceptibilities. From late morning to early afternoon, with deepening of

540   boundary layer and clouds decoupled from surface, LWP susceptibility for thick clouds largely decreases and

541   reaches a daily minimum, which contributes to the largest difference between the thin-to-thin and thick-to-thin

542   categories shown in Fig.5b. From afternoon to evening, with the increase of LWP susceptibility for non-

543 precipitating thick clouds, and the difference between the two categories is less pronounced. These results support

544 our hypothesis that clouds retain the memory of their responses to N_d perturbations from their previous states.
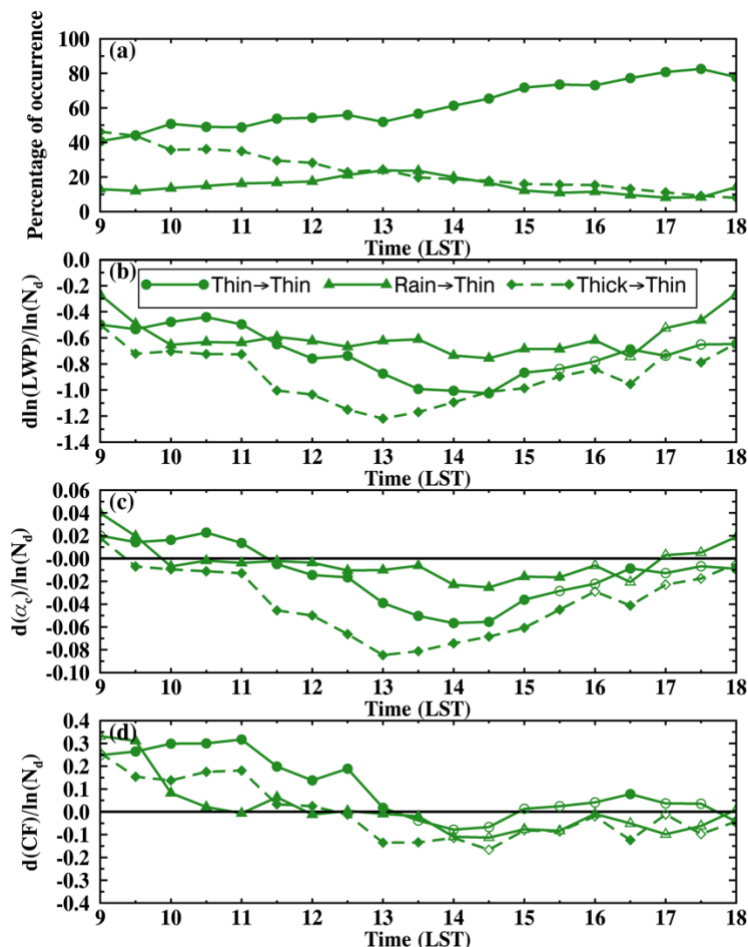
545
546 Figure 5. Daytime variation of non-precipitating thin clouds transition from non-precipitating thin clouds (thin →
547 thin, solid line with circle symbols), precipitating clouds (rain → thin, solid line with triangle symbols), and non-
548 precipitating thick clouds (thick → thin, dashed line with diamond symbols) in previous two hours. Symbols for
549 different state transitions are noted in (b). In (b)-(d), filled markers indicate data points that are significantly
550 different from the other two groups (p<0.05), while open markers indicate statistical insignificance.

551   Similar to LWP, responses of CF to N_d perturbations in the morning retain the memory of the previous

552 state of clouds. As seen in Figure 5d, thin clouds that transitioned from thick clouds or precipitating clouds have

553 significantly less positive CF susceptibility than thin clouds that were previously thin, particularly in the morning.

554 As the CF susceptibility for thin clouds that evolved from precipitating and thick clouds greatly decrease from

555 morning to noon, the CF susceptibility for thin clouds decrease from large positive to near zero from morning to

556 noon (Fig.4c). A maximum in CF susceptibility in the early morning is likely associated with the influence of

557 aerosols on boundary layer mixing and the evolution of boundary layer from morning to noon. The enhanced

558 entrainment rate and radiative cooling rate from N_d perturbations help to destabilize the boundary layer and

559 transport moisture from the ocean surface to clouds, facilitating new cloud formation (e.g., Christensen et al. 2020).

560 As the boundary layer is typically well mixed in the morning with clouds coupled to the surface, the impact of

561 aerosols on CF is strongest in the morning and gradually decrease from morning to noon. In the afternoon, thin

562   clouds transition from all three states have near-zero CF responses to N_d perturbations. Further analyses and model

563   simulations are needed to better understand aerosols' impact and the associated diurnal evolution of entrainment

564   rate, boundary layer mixing, cloud cover and lifetime to explain the observed daytime variation of CF susceptibility

565   for non-precipitating thin clouds.

566   The impact of the cloud memory of AIE on current cloud susceptibility is also evident within a 30-minute

567   window when a transition of cloud state just occurs (Fig.S4). Consistent with the findings in Fig.5, thin clouds that

568   transition from thick clouds exhibit much more negative LWP and α_c susceptibilities compared to thin clouds that

569   remain thin during the 30 minutes. Yet, the number of cases experiencing a transition in cloud state within a 30-

570   miniute window is limited (Fig.S4a). In addition, the impact of the transition in cloud state on the current cloud

571   susceptibility persists for at least four hours (Fig.S5). As our tracking method does not follow individual cloud

572   parcels to track changes in their states, the influence of cloud advection may become significant over longer tracking

573   time, such as four hours. Therefore, a two-hour tracking window is used in this study.

574   As discussed in the method section, while the advective effects in our study are expected to be modest, we

575   further isolate their impact, by performing an analysis for cloud scenes with wind speed of less than 7 m/s (60% of

576   time), when clouds are somewhat stationary in two hours. Influence of transition in cloud state is consistent as in

577   Fig.5 with more negative LWP and α_c susceptibilities for thin clouds transitioned from thick clouds, while the signal

578   is slightly stronger (not shown). This consistency confirms that our tracking method can capture the signal of cloud

579   state transition and its impact on cloud susceptibilities during summer in the study region.

580   In summary, the "U-shaped" daytime variations in LWP and α_c susceptibilities for non-precipitating thin

581   clouds are likely due to cloud retaining the memory of AIE. From morning to noon, as non-precipitating thick

582   clouds evolve to thin clouds, they retain their memory of the large negative LWP susceptibility. Therefore, both

583   LWP and α_c susceptibilities decrease from morning to noon for thin clouds and reach their daily minima at noon. In

584   the afternoon, as a growing percentage of thin clouds persist as thin clouds during the next hours, LWP and α_c

585   susceptibilities gradually increase to less negative and near zero, respectively.

3.4.2 Non-precipitating thick clouds
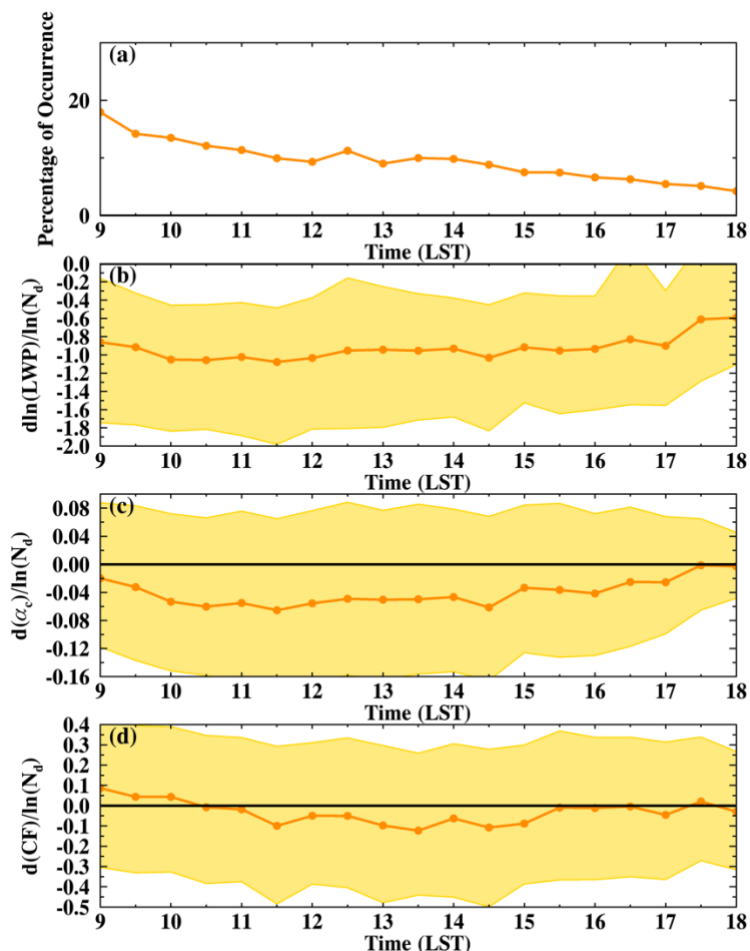
Figure 6. Daytime variation of (a) percentage of occurrence of non-precipitating thick clouds to warm boundary layer clouds, (b) cloud LWP susceptibility ($dln(LWP)/dln(N_d)$), (c) cloud albedo susceptibility ($d\alpha_c/dln(N_d)$), and (d) cloud fraction susceptibility ($dCF/dln(N_d)$) for non-precipitating thick clouds. The shaded areas represent the lower and upper 25th percentile of the cloud susceptibilities for each time step and the solid lines with dots represent the mean values.

Consistent with Fig.2e, non-precipitating thick clouds are the least frequent warm boundary layer cloud state during summer over the ENA region. Their percentage of occurrence continuously decreases from 20% in the morning to less than 5% in the evening (Fig.6a). For LWP and α_c, their susceptibilities first decrease from less negative to more negative in the morning and then increase from noon to evening (Fig.6b and c, respectively). CF susceptibility is weakly positive in the early morning, becomes weakly negative from late morning to early afternoon, and increases to near zero in the evening (Fig.6d). The daytime evolutions of LWP and α_c susceptibilities for thick clouds exhibit consistent trend with cloud susceptibilities for thin clouds transition from thick clouds shown in Fig.5 but with a lag of two hours. For example, the LWP susceptibility for thick clouds decreases from −0.8 to −1.1 from 9 to 11 LST and it increase from −1.1 to −0.8 from 11 to 16 LST; while the LWP susceptibility for the thick-to-thin category in Fig.5b decreases from −0.8 to −1.2 from 11-13 LST and increases to −0.6 from 13 to 18 LST. This result supports our hypothesis on cloud retaining its memory of AIE of its previous cloud state.

22

604   To gain insight into the observed evolution of LWP and α_c susceptibility from morning to evening, we

605   investigate the influence of cloud state transition on cloud susceptibility for non-precipitating thick clouds, which is

606   summarized as H1 in Table 1. As shown in Fig.7a, around 40% of thick clouds sustain as thick clouds from the

607   previous two hours in the morning; whereases during the late afternoon to evening, with decreasing solar radiation,

608   more than 60% of thick clouds are developed from thin clouds. Consistent with the findings presented in Fig.5, thick

609   clouds that are previously thick exhibit significantly more negative LWP susceptibility compared to thick clouds that

610   are previously thin (Fig.7b). These differences are particularly prominent from late morning to noon and become

611   insignificant in the afternoon. As discussed before, difference between the thick-to-thick and the thin-to-thick

612   categories are due to the LWP susceptibilities for thick and thin clouds of previous time, while the smaller

613   differences in the early morning and afternoon could be attributed to the expected stronger turbulence and cloud

614   coupling at these times. Additionally, Fig.7d indicates that transition in cloud state cannot explain the daytime

615   variation in CF susceptibility for thick clouds, as all three groups are insignificantly different from each other.
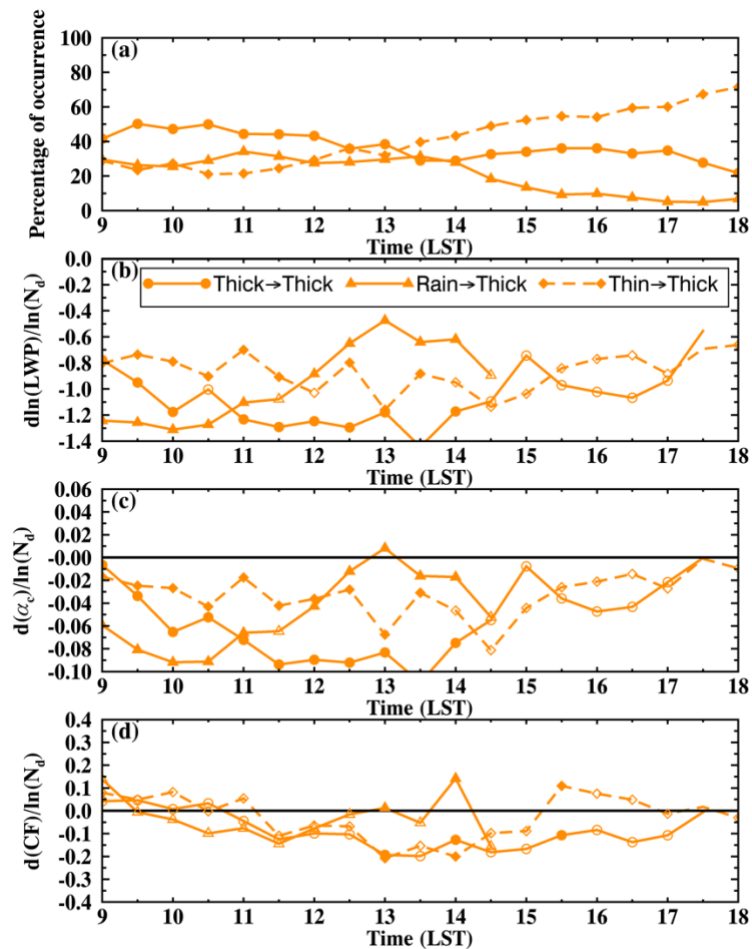
616
617   Figure 7. Daytime variation of non-precipitating thick clouds transition from non-precipitating thick clouds (thick →
618   thick, solid line with circle symbols), precipitating clouds (rain → thick, solid line with triangle symbols), and non-
619   precipitating thin clouds (thin → thick, dash line with diamond symbols) in previous two hours. Symbols for
620   different state transitions are noted in (b). In (b)-(d), filled markers indicate data points that are significantly
621   different from the other two groups (p<0.05), while open markers indicate statistical insignificance.

23

622   To understand the driving mechanism for the daytime variation in CF susceptibility shown in Figure 6d, we
623   calculate the mean cloud properties for non-precipitating thin and thick clouds, as shown in Fig.8. In the morning,
624   non-precipitating thick clouds are predominantly overcast clouds with a mean CF of 75% (Fig.8a). To distinguish
625   between overcast and broken clouds, we calculate the diameter-to-height ratio (DHR) for each cloud, where
626   diameter is estimated by the square root of the area and height is defined as the 90th percentile of cloud tops. As
627   shown in Fig.8c, thick clouds are mostly overcast in the morning with a mean DHR of 230. Compared to broken
628   clouds, overcast clouds have less room for CF to increase, which results in a less positive CF susceptibility for thick
629   clouds compare to thin. After 10 am, non-precipitating thick clouds start to break. The mean CF decreases from 75%
630   at 10 am to 60% at 2 pm and the DHR decreases from 230 to 170. As CF for broken clouds is more sensitive to N_d
631   perturbations, CF susceptibility decreases to $-0.13\ ln(N_d)^{-1}$, which is consistent with the daytime mean negative
632   CF susceptibility shown in Fig.2c. From afternoon to evening, clouds transition to overcast again (Fig.8), and the CF
633   susceptibility increases back to zero. This impact of cloud morphology (e.g., overcast or broken clouds) on daytime
634   variation of CF susceptibility is summarized as H3 in Table 1.
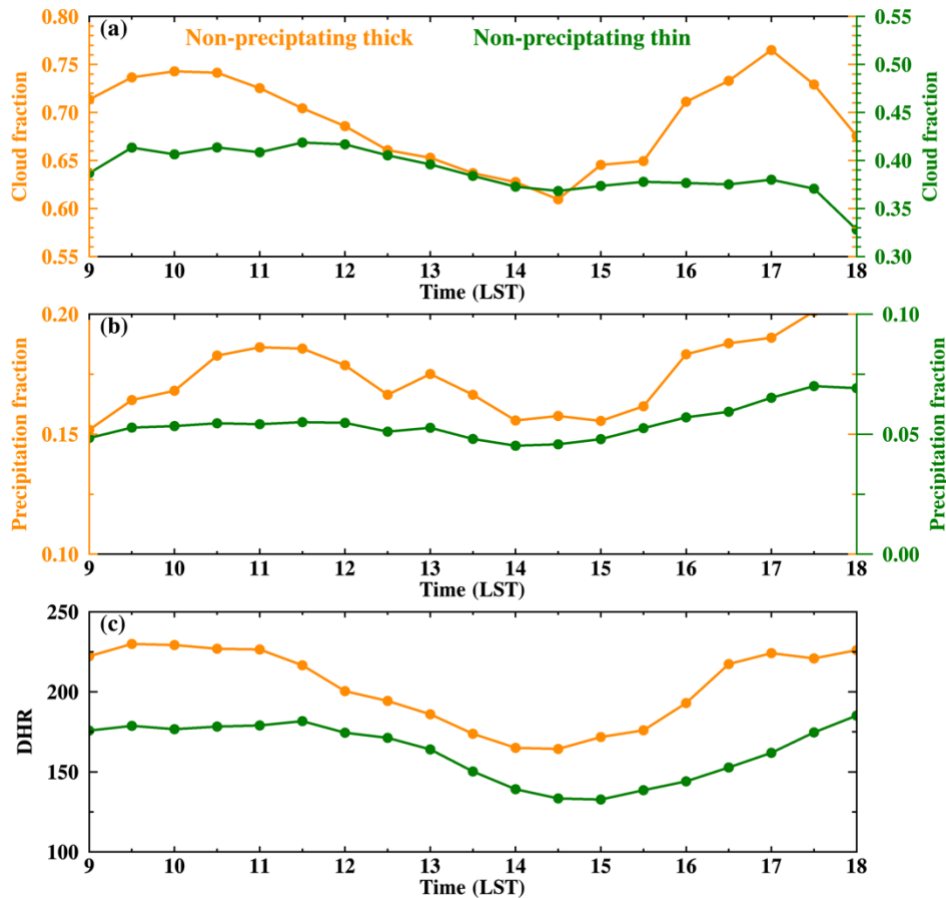
635
636   Figure 8. Diurnal variation of (a) cloud fraction, (b) pixel-level precipitation fraction, and (c) diameter-to-height
637   ratio (DHR) for non-precipitating clouds. Different colors represent different cloud states as indicated in (a). Please
638   note that the non-precipitating thin cloud in (a) and (b) use the y-axis on the right side.

24

639   The previous results are summarized as follows: LWP susceptibility for non-precipitating thick clouds first

640   decreases from less negative to more negative in the morning and then increase from noon to evening, which is

641   likely attributed to the transition from thin to thick clouds. In the morning, 40% to 50% of thick clouds are

642   previously thick clouds, these clouds exhibit a large negative LWP susceptibility. In the afternoon, with increasing

643   percentage of thick clouds develop from thin clouds and retain the memory of LWP susceptibility of thin cloud.

644   LWP susceptibility gradually increases and becomes similar to that of thin clouds (Fig.4b, 6b). Daytime variation in

645   CF susceptibility for thick clouds is likely attributed to changes in cloud morphology. In the morning and evening,

646   thick clouds are mostly overcast with CF less sensitive to N_d perturbations, resulting in a near zero CF

647   susceptibility. From late morning to early afternoon, the overcast thick clouds break down and CF decrease with

648   increasing N_d likely due to the enhanced entrainment and evaporation.

649   The impact of cloud memory and transition of cloud state on the daytime variation of LWP susceptibility is

650   summarized as a schematic figure shown in Fig.9. From morning to noon, as non-precipitating thick clouds

651   transition to thin clouds, thin clouds retain their memory of the large negative LWP susceptibility of their previous

652   state. Therefore, LWP susceptibility for thin clouds decreases from morning to noon and reach its daily minima in

653   the early afternoon. From early afternoon to evening, with non-precipitating thin clouds developing to thick clouds,

654   LWP susceptibility for thick clouds increase.
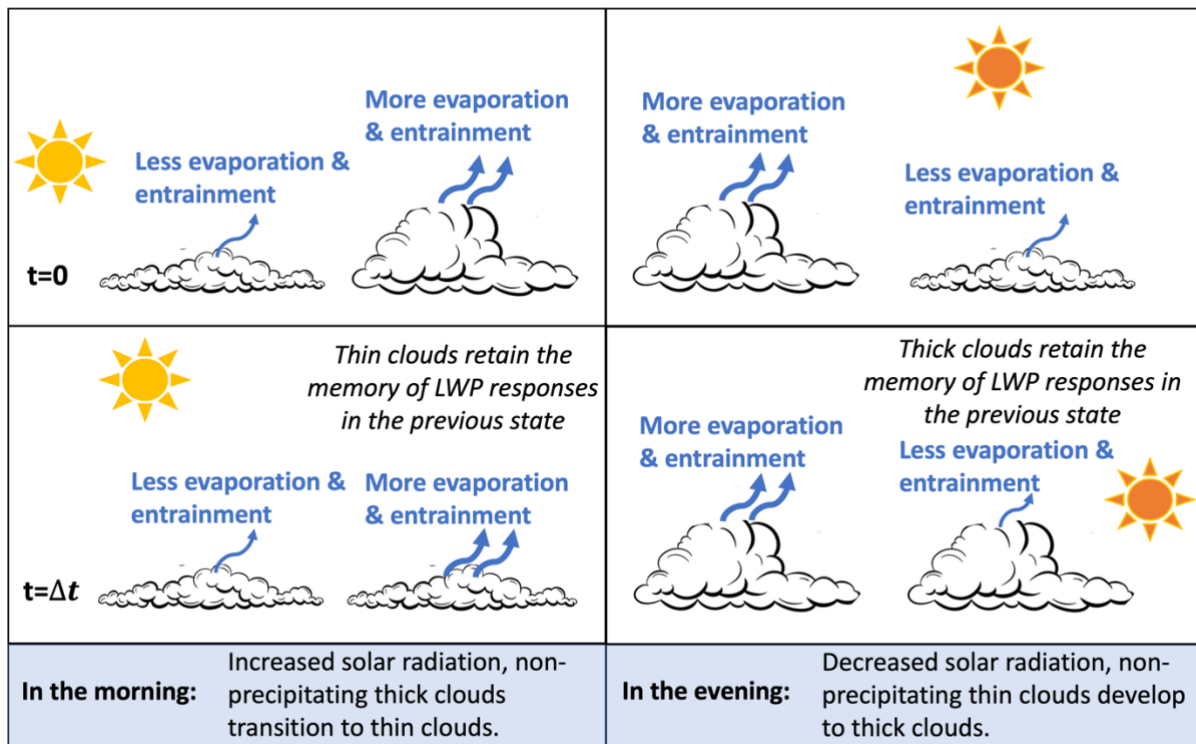
655
656   Figure 9. Schematic figure of influence of cloud memory and transition of cloud state on the LWP susceptibility and
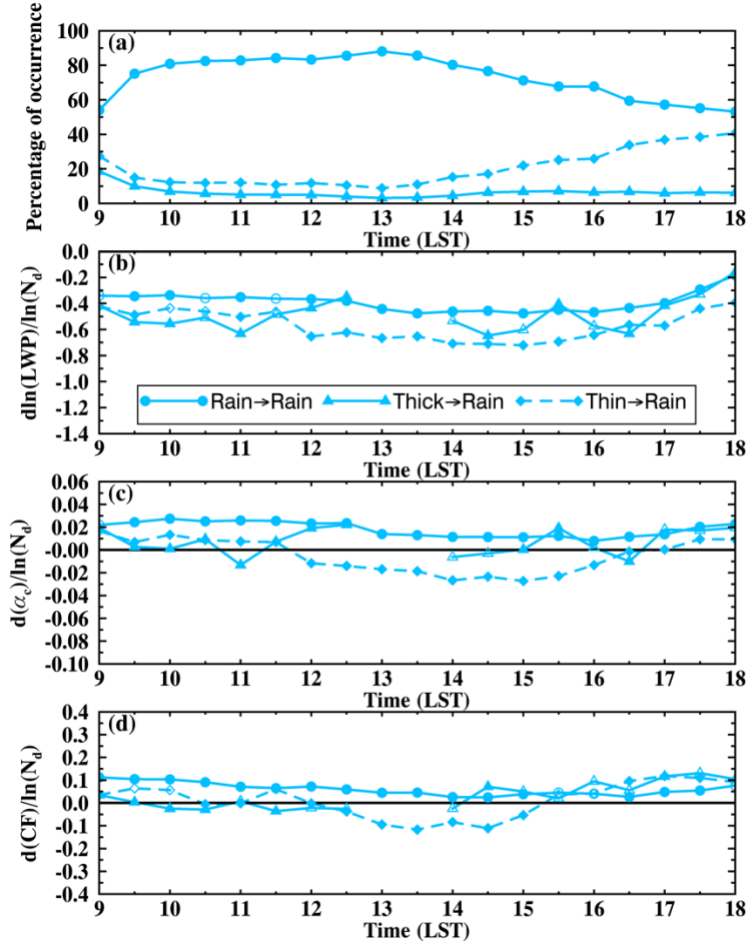657   its daytime variation.

3.4.3 Precipitating clouds
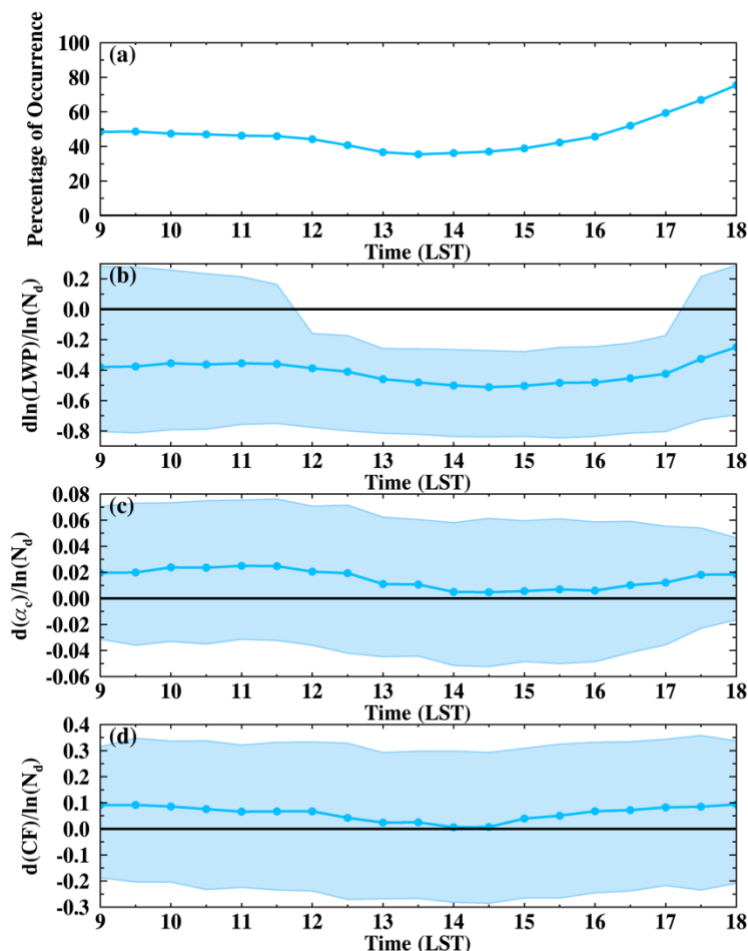
Figure 10. Daytime variation of (a) percentage of occurrence of precipitating clouds to warm boundary layer clouds, (b) cloud LWP susceptibility ($dln(LWP)/dln(N_d)$), (c) cloud albedo susceptibility ($d\alpha_c/dln(N_d)$), and (d) cloud fraction susceptibility ($dCF/dln(N_d)$) for precipitating clouds. The shaded areas represent the lower and upper 25th percentile of the cloud susceptibilities for each time step.

Precipitating clouds, depicted in Figs.10a, are the dominant cloud state in this region, accounting for 46% of the warm boundary layer clouds, compared to 44% of non-precipitating thin clouds. The frequency of precipitating clouds is higher in the morning and evening compared to noon. Throughout the day, the mean LWP susceptibility remain consistently negative, fluctuating between −0.5 to −0.3, with minimum values between 14–16 LST (Figs.10b). The daytime variability in LWP susceptibility for precipitating clouds is much lower than that for non-precipitating thin (e.g., from −0.9 to −0.4) and thick (e.g., from −1.1 to −0.6) clouds. The negative LWP susceptibility is likely due to the prevalence of lightly precipitating clouds, with a mean precipitating fraction ranging from 0.2 to 0.5 (Fig.S2d). The influence of precipitation suppression is smaller than that of the entrainment enhancement. Similarly, α_c susceptibility fluctuates between 0 to 0.02 throughout the day, with near zero α_c susceptibility in early afternoon (Figs.10c). Despite the minimal daytime variation, the LWP and α_c susceptibilities at 13-16 LST are statistically significant different from cloud susceptibilities in the morning and evening at 95%

26

675 confidence level with the two-tailed t-test. The CF susceptibility for precipitating clouds also shows minimal

676 daytime variation compared to non-precipitating clouds, with a mean value ranging from 0 to 0.1 (Figs.10d).

677   Consistent with non-precipitating clouds, the daytime variation of LWP and α_c susceptibilities for

678 precipitating clouds can be attributed to the transition of cloud states. For example, as shown in Figs.11b-d,

679 precipitating clouds that transition from non-precipitating thin clouds exhibit significantly more negative/less

680 positive cloud susceptibilities than precipitating clouds that are previously precipitating. Meanwhile, α_c and CF

681 susceptibilities switch signs from positive to negative in the afternoon for precipitating clouds transition from non-

682 precipitating thin clouds compared to that are previously precipitating (dash line with diamond symbols in Figs. 11c,

683 d). Starting from 13 LST, when non-precipitating thin clouds transition to precipitating clouds (Fig.11a), LWP and

684 α_c susceptibilities begin to decrease and reach their daily minimum in the late afternoon. Interestingly, as non-

685 precipitating clouds transition to precipitating clouds (Figs.11b and c, thin → rain, thick → rain), their LWP and α_c

686 susceptibilities exhibit both less negative values and smaller daytime variations compared to thin/thick clouds that

687 remain as thin/thick (Figs. 5b and c, thin → thin, Figs. 7b and c, thick → thick). The underlying reason for this

688 observation is currently unclear and warrants further investigation on the sensitivity of AIE for clouds experiencing

689 transition in cloud states, especially between precipitating and non-precipitating clouds. Lastly, the percentage of

690 precipitating clouds that transition from non-precipitating thick clouds is less than 7% (Fig.11a).

691   In conclusion, precipitating clouds exhibit smaller daytime variation in cloud susceptibilities compared to

692 non-precipitating thin and thick clouds. The decrease of LWP and α_c susceptibilities for precipitating clouds in the

693 afternoon is likely contributed by the transition of non-precipitating thin clouds to precipitating clouds.

Figure 11. Daytime variation of precipitating clouds transitioned from precipitating clouds (rain → rain, solid line with circle symbols), non-precipitating thick clouds (thick → rain, solid line with triangle symbols), and non-precipitating thin clouds (thin → rain, dash line with diamond symbols) in previous two hours. Symbols for different state transitions are noted in (b). In (b)-(d), filled markers indicate data points that are significantly different from the other two groups (p<0.05), while open markers indicate statistical insignificance.

Combining the results shown here and results in section 3.4.1, we can answer which cloud state contributes the most to the daytime variation of cloud susceptibility. The non-precipitating thin clouds exhibit similar daytime variations in LWP, α_c, and CF susceptibility than the warm boundary layer clouds (Fig.4 vs. Fig.3), with clouds being less susceptible to N_d perturbations in the morning and evening and more susceptible at noon. Additionally, non-precipitating thin clouds have highest frequency at noon. On the other hand, precipitating clouds, despite their higher percentage of occurrence than thin clouds, exhibit minimal daytime variation in cloud susceptibility. Therefore, the pronounced daytime variations in cloud susceptibilities for warm boundary layer clouds primarily stem from non-precipitating thin clouds. The distinct daytime evolution patterns for the three clouds states highlight the importance of cloud state classification in quantification of cloud susceptibility.

3.5 Contribution to the daytime variation of cloud susceptibility

As discussed in the previous section, both the frequency of occurrence of cloud states and the intensity of cloud responses to N_d perturbations exhibit pronounced daytime variations. In this section, we aim to compare the

28

712 contribution of these two components to the overall daytime variation in cloud susceptibilities by fixing one

713 component constant at a time. The contribution from changes in the frequency of cloud states is represented by the

714 red lines in Fig.12, which is estimated by weighting the daytime mean cloud susceptibility (Figs. 2a-c) with the half-

715 hourly frequency of occurrence of clouds in the LWP-N_d parameter space, assuming a constant intensity of cloud

716 susceptibility during the daytime. The contribution from changes in the intensity of cloud susceptibility is depicted

717 by the blue lines, which is estimated by weighting the half-hourly cloud susceptibility in the LWP-N_d parameter

718 space with the daytime mean frequency of occurrence of clouds (Fig.2e), assuming a constant frequency during the

719 daytime. The black line in Fig.12 represents the observed susceptibility shown in Fig.3, and it includes the

720 contributions from daytime variations in both components.
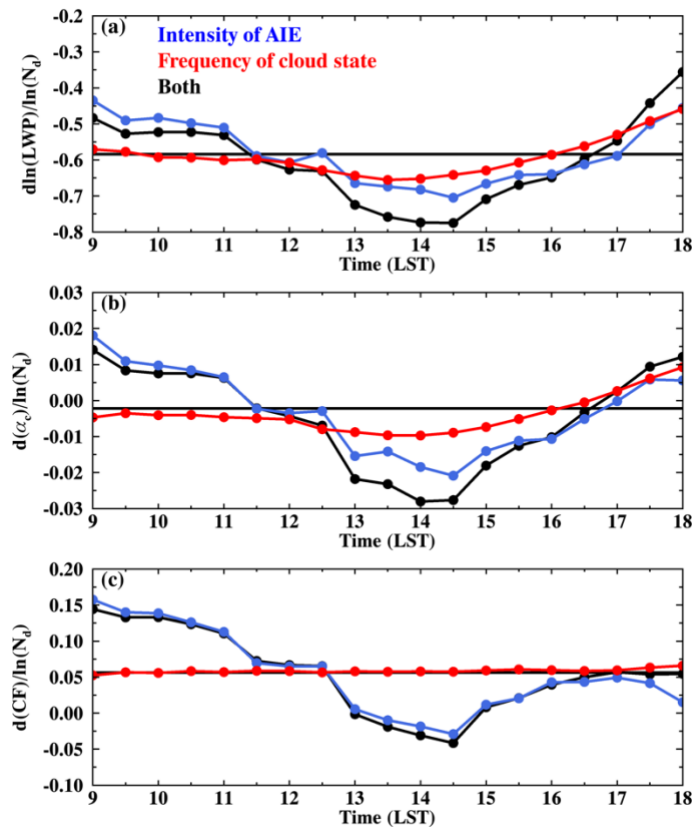
721
722 Figure 12. Daytime variation in cloud susceptibility contributed from the variability in the intensity of susceptibility
723 (blue lines with symbols), variability in the frequency of occurrence of cloud state (red lines with symbols), and
724 from both (black lines with symbols). (a) cloud LWP susceptibility ($dln(LWP)/dln(N_d)$), (b) cloud albedo
725 susceptibility ($d\alpha_c/dln(N_d)$), (c) cloud fraction susceptibility ($dCF/dln(N_d)$). The horizontal black solid lines in
726 (a)-(c) are the daytime mean susceptibility.

727   When comparing the net observed daytime variation of cloud susceptibilities (black lines) with the

728 contributions from changes in the intensity and the frequency of cloud state (blue and red lines, respectively), we

729 find that the daytime changes in cloud susceptibility is primarily driven by changes in the intensity of cloud

730 susceptibilities during the day. Additionally, as shown in Figs. 12a and b, the red lines are close to the daytime mean

731 values in the morning, which indicates that variations in the frequency of different cloud states have minimal impact

732 on changes in LWP and α_c susceptibilities in the morning. On the other hand, in the afternoon, both shifts in cloud

733 states and changes in intensities contribute to the changes in LWP and α_c susceptibilities. Compared with LWP and

734 α_c susceptibilities, the daytime variation of CF susceptibility shows minimal sensitivity to changes in cloud state

735 frequency. This limited impact stems from the fact that the daytime fluctuation in cloud state frequency is

736 predominantly influenced by precipitating and non-precipitating thin clouds. Meanwhile, the daytime mean CF

737 susceptibilities for precipitating and non-precipitating thin clouds closely align, measuring at 0.08 and 0.09,

738 respectively (Fig.2c). This convergence diminishes the influence of alterations in the frequency of these two cloud

739 states.

740   In summary, the daytime variation of cloud susceptibility is largely driven by the variation in its intensity.

741 Since polar-orbiting satellites only observe the cloud responses to N_d perturbations across different cloud states at

742 their overpass time, they cannot fully capture the diurnal variation of cloud susceptibilities driven by the variation in

743 the intensity of cloud susceptibility. Given that all three cloud susceptibilities reach their daily minimum at around

744 13:30 LST, studies based on polar-orbiting satellite with overpass time at noon may underestimate the daily mean

745 value of cloud susceptibility.

746   **4. Discussions**

747   In this study, we quantify the susceptibility of warm boundary layer clouds to N_d perturbation using the

748 pixel-level SEVIRI cloud retrievals of each time step. For heavily precipitating clouds, LWP increases under pristine

749 condition (e.g., $N_d < 30\ cm^{-3}$, Fig.2a). For lightly precipitating and non-precipitating clouds, LWP decreases with

750 N_d. The N_d-LWP relationship found in this study is consistent with that in Gryspeerdt et al. (2019) using global

751 mean cloud retrievals from MODIS and AMSR-E at coarser resolution of $1° \times 1°$ and daily timescale. This

752 consistency between different satellite measurements at different temporal and spatial scales greatly enhance our

753 confidence in the retrieved relationship.

754   This study further distinguishes non-precipitating clouds into thin and thick clouds based on their LWP. A

755 consistent decreasing trend in cloud water is found for both states, yet non-precipitating thick clouds exhibit more

756 negative LWP susceptibility ($\frac{dln(LWP)}{dln(N_d)} = -0.94$) compared to thin clouds ($\frac{dln(LWP)}{dln(N_d)} = -0.71$). The LWP

757 susceptibilities estimated in this study are more negative than those in Zhang et al. (2022) and Zhang and Feingold

758 (2023), based on similar classification of cloud states. Particularly, we found that non-precipitating thin clouds have

759 a decreasing trend in cloud water and a warming effect at the surface radiation while these are opposite in Zhang et

760 al. (2022) and Zhang and Feingold (2023). This is due to different seasons and study regions between our and their

761 studies. The summer boundary layer in the ENA region is deeper and less stable with higher cloud tops (e.g., Klein

762 and Hartmann, 1993; Ding et al., 2021; King et al., 2013) compared to the NE Pacific in Zhang et al. (2022) and the

763 NE Atlantic region in Zhang and Feingold (2023). The less stable condition, deeper boundary layer, and deeper

764 clouds could lead to a stronger cloud-top entrainment rate and result in a more negative LWP susceptibility (Possner

765 et al., 2020; Toll et al., 2019).

766   Regarding the CF adjustment to N_d perturbation, a daytime mean positive response is found for

767 precipitating and non-precipitating thin clouds and a negative response for non-precipitating thick clouds (Fig.2c).

30

768 Few studies have quantified the CF adjustment rate at 30-minute intervals for a direct comparison of CF

769 susceptibility. However, similar results are found using measurements and retrievals from different platforms at

770 various spatial and timescales, which greatly increase our confidence in the observed CF responses toward N_d

771 perturbation. For example, using MODIS measurement, Kaufman et al. (2005) found an increase in the longitudinal

772 mean cloudiness for warm boundary layer clouds with increasing AOD in all four regions of the Atlantic Ocean

773 characterized by distinct aerosol types. Using the natural experiment of volcanic eruption at Holuhraun in Iceland,

774 Chen et al. (2022) found that aerosols from the eruption increase the monthly mean cloud cover by 10% over the

775 North Atlantic. By tracking the cloud trajectory using geostationary satellites, Christensen et al. (2020) found that

776 aerosol enhance both CF and cloud lifetime in the timescale of 2-3 days, especially under stable conditions. It is

777 worth noting that a decrease in CF was not observed in these studies, likely due to the prevalence of non-

778 precipitating thin clouds and precipitating clouds in the Atlantic or the NE Pacific (e.g., Zhang and Feingold, 2023)

779 that mask the signal from non-precipitating thick clouds without distinguishing cloud states.

780 Lastly, the distinct "U-shaped" daytime variation in all three cloud properties found in this study (Fig.3a-c)

781 is *unlikely* due to the systematic bias in r_e and τ retrievals at large SZA based on the following two aspects. Firstly,

782 if the daytime variation is driven by retrieval bias at large SZA, we would expect the susceptibility exhibiting a

783 symmetric pattern at local noon. As shown in Figs. 10 and 6, the LWP and α_c susceptibilities for precipitating and

784 non-precipitating thick clouds exhibit asymmetric pattern at local noon: with a decreasing trend from 13 LST and a

785 daily minimum at 16 LST, and a continuously increasing trend from 11 to 18 LST, respectively. In addition, the CF

786 susceptibilities for all three cloud states show asymmetric patterns at local noon. Secondly, if the retrieval

787 uncertainty dominates the signal, we would expect less variation in cloud susceptibilities for overcast clouds, which

788 suffer less uncertainties in cloud retrievals from the plane-parallel assumption and the cloud 3-D effect. However,

789 the opposite is found from the sensitivity test where overcast clouds exhibit stronger daytime variation in cloud

790 susceptibilities (not shown).

791 **5. Conclusions**

792 Using N_d as an intermediary variable, this study investigates the aerosol indirect effect (AIE) for warm

793 boundary layer clouds and its daytime variation over the ENA region with the half-hourly and 3-km cloud property

794 retrievals from SEVIRI on the Meteosat-11. To constrain meteorological impacts on clouds and aerosol-cloud

795 interaction, cloud susceptibilities are estimated within a $1° \times 1°$ grid box for each satellite time step. Based on the

796 daytime mean cloud susceptibilities in the LWP-N_d parameter space, the sign and magnitude of cloud

797 susceptibilities strongly depend on the cloud states (Fig.2). Accordingly, warm boundary layer clouds are classified

798 into three states: precipitating clouds (r_e>15 μm), non-precipitating thick clouds (r_e<15 μm, LWP > 75 gm^{-2}), and

799 non-precipitating thin clouds (r_e<15 μm, LWP < 75 gm^{-2}).

800 Precipitating clouds exhibit contrasting responses in cloud LWP, with increases observed for heavily

801 precipitating clouds and decreases for lightly precipitating clouds. Positive α_c and CF susceptibilities are identified

802 for both heavily and lightly precipitating clouds. The net all-sky radiative forcing of the AIE on precipitating clouds

31

803   is estimated to be $-13\ W\ m^{-2} ln(N_d)^{-1}$, with contributions from the CF and α_c effects of -9.5 and -3.5

804     $W\ m^{-2}\ ln(N_d)^{-1}$, respectively. For non-precipitating clouds, both thick and thin clouds show negative LWP

805   susceptibility with more negative values found for thick clouds with higher LWP and N_d. This is likely attributed to

806   the larger cloud top radiative cooling rate and stronger entrainment for thick clouds. Consistent with the

807   evaporation-entrainment feedback, non-precipitating thick clouds exhibit a decrease in CF and α_c with increasing

808   N_d, and results in a net warming effect at the surface and a radiative forcing of $+4.4\ W\ m^{-2}\ ln(N_d)^{-1}$. On the other

809   hand, non-precipitating thin clouds show an increasing response in CF and a less negative α_c susceptibility.

810   Additionally, the radiative effect from increasing CF ($-8.3\ W\ m^{-2}\ ln(N_d)^{-1}$) outweighs that from a darker cloud

811   ($+3.1\ W\ m^{-2} ln(N_d)^{-1}$) and leads to a net cooling effect of $-5.2\ W\ m^{-2}\ ln(N_d)^{-1}$.

812   Warm boundary layer clouds manifest distinct and significant ($p<0.05$) daytime variations in LWP, α_c, and

813   CF susceptibilities. All three cloud susceptibilities exhibit "U-shaped" diurnal patterns with clouds being less

814   susceptible in the morning and evening and more susceptible at local noon (Fig.3).

815   Daytime variation in LWP and α_c susceptibilities is likely attributed to the transition in cloud state while

816   clouds sustaining the memory of responses to N_d of the previous state (H1 in Table 1). From morning to noon, with

817   increasing solar radiation, non-precipitating thick clouds evolve to thin clouds. Thin clouds decayed from thick show

818   significantly more negative LWP and α_c susceptibilities than thin clouds that are previously thin (Fig.5). Therefore,

819   LWP and α_c susceptibilities decrease from morning to noon for thin clouds and reach their daily minima at noon

820   (Fig.4). In the afternoon, thin clouds develop to thick clouds while retaining the memory of less susceptible to N_d

821   perturbations (Fig.7) and therefore leads to an increase in LWP and α_c susceptibilities for nonprecipitating thick

822   clouds in the afternoon (Fig.6). Meanwhile, daytime variation in CF susceptibility for non-precipitating thick clouds

823   is more likely driven by changes in cloud morphology rather than the transition of cloud state (Fig.8, H3 in Table 1).

824   Compared to non-precipitating clouds, precipitating clouds exhibit smaller daytime variation in cloud susceptibility

825   (Fig.10).

826   The daytime variation in cloud susceptibility is primarily driven by changes in the intensity of cloud

827   susceptibilities from morning to noon, rather than changes in the frequency of occurrence of different cloud states

828   (Fig.12). As the polar-orbiting satellites only observe cloud susceptibilities across different cloud states during a

829   specific overpass time, they overlook the change in the intensity of cloud susceptibilities during the day. More

830   specifically, based on the daytime variation of cloud susceptibilities found in this study, LWP susceptibility

831   estimated at 13:30 LST could underestimate the daytime mean value by 26.3% (-0.76 compared to -0.60),

832   underestimate the α_c susceptibility by 475% (-0.023 compared to -0.004), and underestimate the CF susceptibility

833   by 120% (-0.019 compared to $+0.055$). It is worth noting that both the daytime variation and the daytime mean

834   values of cloud susceptibilities in this study are estimated based on the regression analysis on spatial data within

835   each satellite time step, with the assumption that the temporal change of cloud properties from N_d perturbations can

836   be represented by the spatial relationships.

837   This study underscores the importance of considering the diurnal cycle of cloud susceptibilities when

838   quantifying AIE and their impacts on clouds and radiation. The classification of cloud states enables us to

839   distinguish the sign, magnitude, and underlying processes driving the diurnal variation of AIE.

840   To further advance our understanding of the diurnal variation of AIE, several avenues for future research
841   can be pursued. Firstly, it is important to address uncertainties associated with satellite retrievals, which can
842   propagate into uncertainties in the retrieved N_d, as discussed in Grosvenor et al. (2018). Future study could utilize
843   active sensors to reduce these uncertainties, particularly during nighttime conditions. Moreover, using the retrieved
844   N_d as a proxy of aerosol concentration may introduce uncertainties related to cloud processes that can act as sources
845   or sinks of N_d, potentially buffer the relationships between N_d and cloud condensation nuclei. Future investigations
846   are needed to better understand the relationships, and how they vary with different cloud processes and throughout
847   the day. Lastly, this study encompasses all warm boundary layer clouds without considering the highly diverse
848   meteorological regimes and the associated cloud types in the ENA region. Classification of the synoptic and
849   meteorological conditions associated with different cloud states and aerosol properties would contribute to a more
850   comprehensive understanding, allowing for the disentanglement of the impacts of meteorology from AIE.

851

852

872

Competing interests:

The authors declare that they have no conflict of interest.

875

876

877 **References**

878 Albrecht, B. A.: Aerosols, Cloud Microphysics, and Fractional Cloudiness, Science, 245, 1227–1230,

879   https://doi.org/10.1126/science.245.4923.1227, 1989.

880 Arola, A., Lipponen, A., Kolmonen, P., Virtanen, T. H., Bellouin, N., Grosvenor, D. P., Gryspeerdt, E., Quaas, J., &

881   Kokkola, H. (2022). Aerosol effects on clouds are concealed by natural cloud heterogeneity and satellite

882   retrieval errors. Nature Communica)ons, 13(1), 7357. hrps://doi.org/10.1038/s41467-022-34948-5Bennartz, R.:

883   Global assessment of marine boundary layer cloud droplet number concentration from satellite, J. Geophys.

884   Res.,112, D02201, doi:10.1029/2006JD007547, 2007.

885 Bennartz, R. and Rausch, J.: Global and regional estimates of warm cloud droplet number concentration based on 13

886   years of AQUA-MODIS observations, Atmos. Chem. Phys., 17, 9815–9836, https://doi.org/10.5194/acp-17-

887   9815-2017, 2017.

888 Bréon, F.-M., Tanré, D., and Generoso, S.: Aerosol effect on cloud droplet size monitored from satellite, Science,

889   295, 834–838, 2002.

890 Bretherton, C. S., Blossey, P. N., and Uchida, J.: Cloud droplet sedimentation, entrainment efficiency, and

891   subtropical stratocumulus albedo, Geophys. Res. Lett., 34, L03813, https://doi.org/10.1029/2006GL027648,

892   2007.

893 Brenguier, J. L., Burnet, F., & Geoffroy, O.: Cloud optical thickness and liquid water path – does the coefficient

894   vary with droplet concentration? *Atmospheric Chemistry and Physics*, *11*(18), 9771-9786.

895   https://doi.org/10.5194/acp-11-9771-2011, 2011

896 Chen, Y.-C., Christensen, M., Stephens, G. L., and Seinfeld, J. H.: Satellite-based estimate of global aerosol–cloud

897   radiative forcing by marine warm clouds, Nature Geosci., 7, 643–646, https://doi.org/10.1038/ngeo2214, 2014.

898 Chen, Y., Haywood, J., Wang, Y., Malavelle, F., Jordan, G., Partridge, D., Fieldsend, J., De Leeuw, J., Schmidt, A.,

899   Cho, N., Oreopoulos, L., Platnick, S., Grosvenor, D., Field, P., & Lohmann, U.: Machine learning reveals

900   climate forcing from aerosols is dominated by increased cloud cover. *Nature Geoscience*, *15*(8), 609-614, 2022.

901   https://doi.org/10.1038/s41561-022-00991-6

902 Christensen, M. W., Jones, W. K., and Stier, P.: Aerosols enhance cloud lifetime and brightness along the stratus-

903   tocumulus transition, P. Natl. Acad. Sci. USA, 117, 17591–17598, https://doi.org/10.1073/pnas.1921231117,

904   2020.

905 Comstock, K. K., Wood, R., Yuter, S. E., and Bretherton, C. S.: Reflectivity and rain rate in and below drizzling

906   stratocumulus, Q. J. Roy. Meteorol. Soc., 130, 2891–2918, doi:10.1256/qj.03.187, 2004.

907 Ding, F., Iredell, L., Theobald, M., Wei, J., & Meyer, D. :. PBL Height From AIRS, GPS RO, and MERRA-2

908   Products in NASA GES DISC and Their 10-Year Seasonal Mean Intercomparison. *Earth and Space Science*,

909   *8*(9). https://doi.org/10.1029/2021ea001859, 2021

910 Dong, X., Xi, B., Kennedy, A., Minnis, P., & Wood, R.: A 19-month record of marine aerosol–cloud–radiation

911   properties derived from DOE ARM mobile facility deployment at the Azores. Part I: Cloud fraction and single-

912   layered MBL cloud properties. Journal of Climate, 27(10), 3665–3682. https://doi.org/10.1175/JCLI-D-13-

913   00553.1, 2014.

914 Dong, X., Xi, B., Qiu, S., Minnis, P., Sun-Mack, S., & Rose, F. : A radiation closure study of Arctic stratus cloud
915   microphysical properties using the collocated satellite-surface data and Fu-Liou radiative transfer model.
916   *Journal of Geophysical Research: Atmospheres*, *121*(17), 10,175-110,198.
917   https://doi.org/10.1002/2016jd025255, 2016

918 Dong, X., Zheng, X., Xi, B., & Xie, S.: A Climatology of Midlatitude Maritime Cloud Fraction and Radiative Effect
919   Derived from the ARM ENA Ground-Based Observations. Journal of Climate, 36(2), 531–546,
920   https://doi.org/10.1175/JCLI-D-22-0290.1, 2023.

921 Duong, H. T., Sorooshian, A., and Feingold, G.: Investigating potential biases in observed and modeled metrics of
922   aerosol-cloud precipitation interactions, Atmos. Chem. Phys., 11, 4027–4037, doi:10.5194/acp-11-4027-2011,
923   2011.

924 Fan, J. W., Wang, Y., Rosenfeld, D., and Liu, X. H.: Review of aerosol-cloud interactions: mechanisms,
925   significance, and challenges, J. Atmos. Sci., 73, 4221–4252, 2016.

926 Feingold G, Eberhard W, Veron D, Previdi M. First measurements of the Twomey indirect effect using ground-
927   based remote sensors. Geophys Res Lett. 30 (6). https://doi.org/10.1029/2002GL016633, 2003.

928 Feingold, G., Goren, T., & Yamaguchi, T. (2022). Quantifying albedo susceptibility biases in shallow clouds.
929   Atmospheric Chemistry and Physics, 22(5), 3303–3319. https://doi.org/10.5194/acp-22-3303-2022.

930 Glassmeier, F., Hoffmann, F., Johnson, J. S., Yamaguchi, T., Carslaw, K. S., and Feingold, G.: Aerosol-cloud-
931   climate cooling overestimated by ship-track data, Science, 371, 485–489,
932   https://doi.org/10.1126/science.abd3980, 2021.

933 Grosvenor, D. P., & Wood, R.: The effect of solar zenith angle on MODIS cloud optical and microphysical
934   retrievals within marine liquid water clouds. *Atmospheric Chemistry and Physics*, *14*(14), 7291-7321.
935   https://doi.org/10.5194/acp-14-7291-2014, 2014

936 Grosvenor, D. P., Sourdeval, O., Zuidema, P., Ackerman, A., Alexandrov, M. D., Bennartz, R., Boers, R., Cairns,
937   B., Chiu, J. C., Christensen, M., Deneke, H., Diamond, M., Feingold, G., Fridlind, A., HÃOEnerbein, A., Knist,
938   C., Kollias, P., Marshak, A., McCoy, D., Merk, D., Painemal, D., Rausch, J., Rosenfeld, D., Russchenberg, H.,
939   Seifert, P., Sinclair, K., Stier, P., van Diedenhoven, B., Wendisch, M., Werner, F., Wood, R., Zhang, Z., and
940   Quaas, J.: Remote Sensing of Droplet Number Concentration in Warm Clouds: A Review of the Current State
941   of Knowledge and Perspectives, Rev. Geophys., 56, 409–453, https://doi.org/10.1029/2017RG000593, 2018.

942 Gryspeerdt, E., Quaas, J., and Bellouin, N.: Constraining the aerosol influence on cloud fraction, J. Geophys. Res.-
943   Atmos., 121, 3566– 3583, https://doi.org/10.1002/2015JD023744, 2016.

944 Gryspeerdt, E., Goren, T., Sourdeval, O., Quaas, J., Mülmenst.dt, J., Dipu, S., Unglaub, C., Gettelman, A., and
945   Christensen, M.: Constraining the aerosol influence on cloud liquid water path, Atmos. Chem. Phys., 19, 5331–
946   5347, https://doi.org/10.5194/acp-19-5331-2019, 2019.

947 Gryspeerdt, E., Goren, T., and Smith, T. W. P.: Observing the timescales of aerosol–cloud interactions in snapshot
948   satellite images, Atmos. Chem. Phys., 21, 6093–6109, https://doi.org/10.5194/acp-21-6093-2021, 2021.

949 Gryspeerdt, E., McCoy, D. T., Crosbie, E., Moore, R. H., Nott, G. J., Painemal, D., Small-Griswold, J., Sorooshian,
950   A., and Ziemba, L.: The impact of sampling strategy on the cloud droplet number concentration estimated from
951   satellite data, Atmos.Meas. Tech., 15, 3875–3892, https://doi.org/10.5194/amt-15-3875-2022, 2022.

952 Han, Q., Rossow, W. B., Zeng, J., and Welch, R.: Three Different Behaviors of Liquid Water Path of Water Clouds
953   in Aerosol–Cloud Interactions, J. Atmos. Sci., 59, 726–735, https://doi.org/10.1175/1520-
954   0469(2002)059<0726:TDBOLW>2.0.CO;2, 2002.

955 Kaufman, Y. J., Koren, I., Remer, L. A., Rosenfeld, D., & Rudich, Y.: The effect of smoke, dust, and pollution
956   aerosol on shallow cloud development over the Atlantic Ocean. *Proc Natl Acad Sci U S A*, *102*(32), 11207-
957   11212. https://doi.org/10.1073/pnas.0505191102, 2005

958 King, M. D., Platnick, S., Menzel, W. P., Ackerman, S. A., & Hubanks, P. A.: Spatial and Temporal Distribution of
959   Clouds Observed by MODIS Onboard the Terra and Aqua Satellites. *IEEE Transactions on Geoscience and
960   Remote Sensing*, *51*(7), 3826-3852. https://doi.org/10.1109/tgrs.2012.2227333, 2013

961 Klein, S. A., & Hartmann, D. L.: The seasonal cycle of low stratiform clouds. Journal of Climate, 6(8), 1587–1606.
962   https://doi.org/10.1175/1520-0442(1993)006<1587:tscols>2.0.co;2, 1993.

963 Liu, J., Li, Z., and Cribb, M.: Response of marine boundary layer cloud properties to aerosol perturbations
964   associated with meteorological conditions from the 19-month AMF-Azores campaign, J. Atmos. Sci., 73, 4253–
965   4268, https://doi.org/10.1175/JAS-D- 15-0364.1, 2016.

966 Mather, J. H., & Voyles, J. W.: The Arm Climate Research Facility: A Review of Structure and Capabilities, *Bull.
967   Am. Meteorol. Soc.*, 94, 377-392, https://doi.org/10.1175/BAMS-D-11- 00218.1, 2013.

968 Mechem, D. B., Wittman, C. S., Miller, M. A., Yuter, S. E., and De Szoeke, S. P.: Joint synoptic and cloud
969   variability over the Northeast Atlantic near the Azores, J. Appl. Meteorol. Clim., 57, 1273–1290, 2018.

970 Minnis, P., Sun-Mack, S., Young, D. F., Heck, P. W., Garber, D. P., Chen, Y., Spangenberg, D. A., Arduini, R. F.,
971   Trepte, Q. Z., Smith, W. L., Ayers, J. K., Gibson, S. C., Miller, W. F., Hong, G., Chakrapani, V., Takano, Y.,
972   Liou, K., Xie, Y., and Yang, P.: CERES edition-2 cloud property retrievals using TRMM VIRS and Terra and
973   Aqua MODIS data–Part I: Algorithms, IEEE Trans. Geosci. Remote Sens., 49, 4374–4400,
974   https://doi.org/10.1109/TGRS.2011.2144601, 2011.

975 Minnis, P., K. Bedka, Q. Trepte, C. R. Yost, S. T. Bedka, B. Scarino, K. Khlopenkov, and M. M. Khaiyer: A
976   consistent long-term cloud and clear-sky radiation property dataset from the Advanced Very High Resolution
977   Radiometer (AVHRR). Climate Algorithm Theoretical Basis Document (C-ATBD), CDRP-ATBD-0826 Rev 1
978   - NASA, NOAA CDR Program, 159 pp., DOI:10.789/V5HT2M8T,
979   https://www1.ncdc.noaa.gov/pub/data/sds/cdr/CDRs/AVHRR_Cloud_Properties_NASA/AlgorithmDescription
980   _01B-30b.pdf, 2016.

981 Minnis, P., Sun-Mack, S., Chen, Y., Chang, F., Yost, C. R., Smith, W. L., Heck, P. W., Arduini, R. F., Bedka, S. T.,
982   Yi, Y., Hong, G., Jin, Z., Painemal, D., Palikonda, R., Scarino, B. R., Spangenberg, D. A., Smith, R. A., Trepte,
983   Q. Z., Yang, P., and Xie, Y.: CERES MODIS Cloud Product Retrievals for Edition 4–Part I: Algorithm
984   Changes, IEEE T. Geosci. Remote, 11152, 1–37, https://doi.org/10.1117/12.2532931, 2020.

985   Morrison, H., van Lier-Walqui, M., Fridlind, A. M., Grabowski, W. W., Harrington, J. Y., Hoose, C., et al.:
986   Confronting the challenge of modeling cloud and precipitation microphysics. Journal of Advances in Modeling
987   Earth Systems, 12, e2019MS001689. https://doi.org/10.1029/2019MS001689, 2020.

988   Painemal, D., Minnis, P., and Sun-Mack, S.: The impact of horizontal heterogeneities, cloud fraction, and liquid
989   water path on warm cloud effective radii from CERES-like Aqua MODIS retrievals, Atmos. Chem. Phys., 13,
990   9997–10003, https://doi.org/10.5194/acp-13-9997-2013, 2013.

991   Painemal, D.: Global Estimates of Changes in Shortwave Low-Cloud Albedo and Fluxes Due to Variations in Cloud
992   Droplet Number Concentration Derived From CERES-MODIS Satellite Sensors, Geophys. Res. Lett., 45,
993   9288–9296, https://doi.org/10.1029/2018GL078880, 2018.

994   Painemal, D., Spangenberg, D., Smith Jr.,W. L., Minnis, P., Cairns, B., Moore, R. H., Crosbie, E., Robinson, C.,
995   Thornhill, K. L., Winstead, E. L., and Ziemba, L.: Evaluation of satellite retrievals of liquid clouds from the
996   GOES-13 imager and MODIS over the midlatitude North Atlantic during the NAAMES campaign, Atmos.
997   Meas. Tech., 14, 6633–6646, https://doi.org/10.5194/amt-14-6633-2021, 2021.

998   Penner, J. E., Dong, X., and Chen, Y.: Observational evidence of a change in radiative forcing due to the indirect
999   aerosol effect, Nature, 427, 231–234, 2004.

1000   Possner, A., Eastman, R., Bender, F., & Glassmeier, F.: Deconvolution of boundary layer depth and aerosol
1001   constraints on cloud water path in subtropical stratocumulus decks. *Atmospheric Chemistry and Physics*, *20*(6),
1002   3609-3621. https://doi.org/10.5194/acp-20-3609-2020, 2020

1003   Rémillard, J., Kollias, P., Luke, E., and Wood, R.: Marine Boundary Layer Cloud Observations in the Azores, J.
1004   Climate, 25, 7381–7398, https://doi.org/10.1175/JCLI-D-11-00610.1, 2012.

1005   Sandu, I., Brenguier, J., Geoffroy, O., Thouron, O., and Masson, V.: Aerosol impacts on the diurnal cycle of marine
1006   stratocumulus, J. Atmos. Sci., 65, 2705–2718, 2008.

1007   Sandu, I., Brenguier, J.-L., Thouron, O., and Stevens, B.: How important is the vertical structure for the
1008   representation of aerosol impacts on the diurnal cycle of marine stratocumulus? Atmos. Chem. Phys., 9, 4039–
1009   4052, doi:10.5194/acp-9-4039-2009, 2009.

1010   Sato, Y., Goto, D., Michibata, T., Suzuki, K., Takemura, T., Tomita, H., and Nakajima, T.: Aerosol effects on cloud
1011   water amounts were successfully simulated by a global cloud-system resolving model, Nat. Commun., 9, 985,
1012   https://doi.org/10.1038/s41467-018-03379-6, 2018.

1013   Small, J., Chuang, P., Feingold, G. & Jiang, H.: Can aerosol decrease cloud lifetime? Geophys. Res. Lett. 36,
1014   L16806, 2009.

1015   Stevens, B. and Feingold, G.: Untangling aerosol effects on clouds and precipitation in a buffered system, Nature,
1016   461, 607–613, doi:10.1038/nature08281, 2009.

1017   Stevens, B. & Seifert, A.: Understanding the macrophysical outcomes of microphysical choices in simulations of
1018   shallow cumulus convection. J. Meteorol. Soc. Jpn 86A, 141–163, 2008.

1019   Sun-Mack, S., Minnis, P., Chen, Y., Kato, S., Yi, Y., Gibson, S. C., et al.: Regional apparent boundary layer lapse
1020   rates determined from CALIPSO and MODIS data for cloud-height determination. Journal of Applied
1021   Meteorology and Climatology, 53(4), 990–1011, 2014.

Terai, C. R., Wood, R., Leon, D. C., and Zuidema, P.: Does precipitation susceptibility vary with increasing cloud thickness in marine stratocumulus? Atmos. Chem. Phys., 12, 4567–4583, doi:10.5194/acp-12-4567-2012, 2012.

Terai, C. R., Wood, R., and Kubar, T. L.: Satellite estimates of precipitation susceptibility in low-level marine stratiform clouds, J. Geophys. Res., 120, 8878–8889, doi:10.1002/2015JD023319, 2015.

Toll, V., Christensen, M., Quaas, J., and Bellouin, N.: Weak average liquid-cloud-water response to anthropogenic aerosols, Nature, 572, 51–55, https://doi.org/10.1038/s41586-019-1423-9, 2019.

Trepte, Q. Z., and Coauthors: Global cloud detection for CERES edition 4 using Terra and Aqua MODIS data. IEEE Trans. Geosci. Remote Sens., 57, 9410–9449, https://doi.org/10.1109/TGRS.2019.2926620, 2019.

Twomey, S.: The Influence of Pollution on the Shortwave Albedo of Clouds, J. Atmos. Sci., 34, 1149–1152, https://doi.org/10.1175/1520-0469(1977)034<1149:TIOPOT>2.0.CO;2, 1977.

Wang, S., Wang, Q., and Feingold, G.: Turbulence, Condensation, and Liquid Water Transport in Numerically Simulated Nonprecipitating Stratocumulus Clouds, J. Atmos. Sci., 60, 262–278, https://doi.org/10.1175/1520-0469(2003)060<0262:TCALWT>2.0.CO;2, 2003.

Wang, Y., Zheng, X., Dong, X., Xi, B.,Wu, P., Logan, T., and Yung, Y. L.: Impacts of long-range transport of aerosols on marineboundary-layer clouds in the eastern North Atlantic, Atmos. Chem. Phys., 20, 14741–14755, https://doi.org/10.5194/acp-20-14741-2020, 2020.

Warren, S. G., C. J. Hahn, J. London, R. M. Chervine, and R. L. Jenne: Global distribution of total cloud cover and cloud type amounts over ocean, Tech. Note NCAR/TN-317 + STR, 42, Natl. Cent. for Atmos. Res., Boulder, Colo., https://doi.org/10.2172/5415329, 1988.

Williams, A. S., & Igel, A. L.: Cloud top radiative cooling rate drives non-precipitating stratiform cloud responses to aerosol concentration. Geophysical Research Letters, 48, e2021GL094740. https://doi.org/10.1029/2021GL094740, 2021.

Wood, R.: Stratocumulus Clouds, Mon. Weather Rev., 140, 2373–2423, https://doi.org/10.1175/MWR-D-11-00121.1, 2012.

Wu, P., Dong, X., Xi, B., Tian, J., & Ward, D. M.: Profiles of MBL cloud and drizzle microphysical properties retrieved from ground-based observations and validated by aircraft in situ measurements over the Azores. Journal of Geophysical Research: Atmospheres, 125, e2019JD032205. https://doi.org/10.1029/2019JD032205, 2020.

Wu, P., X. Dong, and B. Xi: A climatology of marine boundary layer cloud and drizzle properties derived from ground-based observations over the Azores. J. Climate, 33, 10133–10148, https://doi.org/10.1175/JCLI-D-20-0272.1, 2020.

Xi, B., Dong, X., Minnis, P., & Khaiyer, M. M.: A 10 year climatology of cloud fraction and vertical distribution derived from both surface and GOES observations over the DOE ARM SPG site. *Journal of Geophysical Research*, *115*(D12). https://doi.org/10.1029/2009jd012800, 2010

Xue, H. and Feingold, G.: Large-Eddy Simulations of Trade Wind Cumuli: Investigation of Aerosol Indirect Effects, J. Atmos. Sci., 63, 1605–1622, https://doi.org/10.1175/JAS3706.1, 2006.

Yeom, J. M., Yum, S. S., Shaw, R. A., La, I., Wang, J., Lu, C., et al.: Vertical variations of cloud microphysical relationships in marine stratocumulus clouds observed during the ACE ENA campaign. Journal of Geophysical Research: Atmospheres, 126, e2021JD034700. https://doi.org/10.1029/2021JD034700, 2021.

Zhang, Z., Song, Q., Mechem, D. B., Larson, V. E., Wang, J., Liu, Y., Witte, M. K., Dong, X., and Wu, P.: Vertical dependence of horizontal variation of cloud microphysics: observations from the ACE-ENA field campaign and implications for warm-rain simulation in climate models, Atmos. Chem. Phys., 21, 3103–3121, https://doi.org/10.5194/acp-21-3103-2021, 2021.

Zhang, J., Zhou, X., Goren, T., and Feingold, G.: Albedo susceptibility of northeastern Pacific stratocumulus: the role of covarying meteorological conditions, Atmos. Chem. Phys., 22, 861–880, https://doi.org/10.5194/acp-22-861-2022, 2022.

Zhang, J., and Feingold, G.: Distinct regional meteorological influences on low-cloud albedo susceptibility over global marine stratocumulus regions, Atmos. Chem. Phys., 23, 1073–1090, https://doi.org/10.5194/acp-23-1073-2023, 2023.

Zheng, Q., and Miller, M. A.: Summertime Marine Boundary Layer Cloud, Thermodynamic, and Drizzle Morphology over the Eastern North Atlantic: A Four-Year Study, J. Climate, 35, 4805-4825, https://doi.org/10.1175/JCLI-D-21-0568.1, 2022.

Zheng, X. J., B. K. Xi, X. Q. Dong, P. Wu, T. Logan, and Y. Wang, 2022: Environmental effects on aerosol–cloud interaction in non-precipitating marine boundary layer (MBL) clouds over the eastern North Atlantic. Atmospheric Chemistry and Physics, 22, 335−354, https://doi.org/10.5194/acp-22-335-2022.

Zhou, X., Zhang, J., & Feingold, G.: On the importance of sea surface temperature for aerosol-induced brightening of marine clouds and implications for cloud feedback in a future warmer climate. Geophysical Research Letters, 48, e2021GL095896. https://doi org/10.1029/2021GL095896, 2021.

Zhou, X., & Feingold, G. (2023). Impacts of mesoscale cloud organization on aerosol-induced cloud water adjustment and cloud brightness. Geophysical Research Letters, 50, e2023GL103417. https://doi.org/10.1029/2023GL103417

Zuidema, P., Leon, D., Pazmany, A., & Cadeddu, M.: Aircraft millimeter-wave passive sensing of cloud liquid water and water vapor during VOCALS-REx. *Atmospheric Chemistry and Physics*, *12*(1), 355-369. https://doi.org/10.5194/acp-12-355-2012, 2012